Environmental Fluid Mechanics (2020) 20:1383–1416
https://doi.org/10.1007/s10652-020-09749-3

REVIEW ARTICLE

Undular and broken surges in dam-break flows: a review of wave breaking strategies in a Boussinesq-type framework

Oscar Castro-Orgaz[1] · **Hubert Chanson**[2]

Received: 11 November 2019 / Accepted: 23 May 2020 / Published online: 17 June 2020

Abstract
The water waves resulting from the collapse of a dam are important unsteady free surface flows in civil and environmental engineering. Considering the basic case of ideal dam break waves in a horizontal and rectangular channel the wave patterns observed experimentally depends on the initial depths downstream (h_d) and upstream (h_o) of the dam. For $r = h_d/h_o$ above the transition domain 0.4–0.55, the surge travelling downstream is undular, a feature described by the dispersive Serre–Green–Naghdi (SGN) equations. In contrast, for r below this transition domain, the surge is broken and it is well described by the weak solution of the Saint–Venant equations, called Shallow Water Equations (SWE). Hybrid models combining SGN–SWE equations are thus used in practice, typically implementing wave breaking modules resorting to several criteria to define the onset of breaking, frequently involving case-dependent calibration of parameters. In this work, a new set of higher-order depth-averaged non-hydrostatic equations is presented. The equations consist in the SGN equations plus additional higher-order contributions originating from the variation with elevation of the velocity profile, modeled here with a Picard iteration of the potential flow equations. It is demonstrated that the higher-order terms confer wave breaking ability to the model without using any empirical parameter, such while, for $r > 0.4$–0.55, the model results are essentially identical to the SGN equations but, for $r < 0.4$–0.55, wave breaking is automatically accounted for, thereby producing broken waves as part of the solution. The transition from undular to broken surges predicted by the high-order equations is gradual and in good agreement with experimental observations. Using the solution of the new higher-order equations it was further developed a new wave breaking index based on the acceleration at the free surface to its use in hybrid SGN–SWE models.

Keywords Dam-break wave · Saint–Venant equations · Serre–Green–Nagdhi equations · Positive surge · Wave breaking

✉ Oscar Castro-Orgaz
ag2caoro@uco.es

Hubert Chanson
h.chanson@uq.edu.au

[1] University of Cordoba, Spain, Campus Rabanales, Leonardo Da Vinci Building, 14071 Cordoba, Spain

[2] The University of Queensland, School of Civil Engineering, Brisbane, QLD 4072, Australia

1 Introduction

Dam break flows counts amount the most important types of water waves in civil and environmental engineering, given the potential impact in terms of risk to human life, environmental degradation and economical losses. Before conducting real-life simulations of dam break flows it is mandatory to investigate the behavior of hydraulic models under idealized conditions, namely for an instantaneous removal of a vertical barrier in a horizontal channel under potential flow conditions [1]. Most hydraulic models used to predict dam break waves rely on the Saint–Venant equations [2] or Shallow Water equations (SWE) (Fig. 1a). This is a well-known system of two hyperbolic equations that produce as part of the dam break flow solution continuous (rarefaction) and discontinuous (shock) waves [3, 4]. The shock wave is called in hydraulic "surge", which is as it will be called herein the shock advancing in the positive x direction over the initially motionless fluid with depth h_d [5]. However, hydraulic experimentation indicates that this dispersionless system of equations is not able to predict the detailed wave flow patterns for an arbitrary value of the tailwater flow depth h_d.

Let h_o be the initial water depth upstream in the reservoir, wave breaking occurs in a transition zone for the depth ratio $r = h_d/h_o$, dependent on various factors as boundary friction, channel slope, gate opening time, type of failure, among others. A reasonable interval for threshold ratio is from 0.45 to 0.55 [6–15].

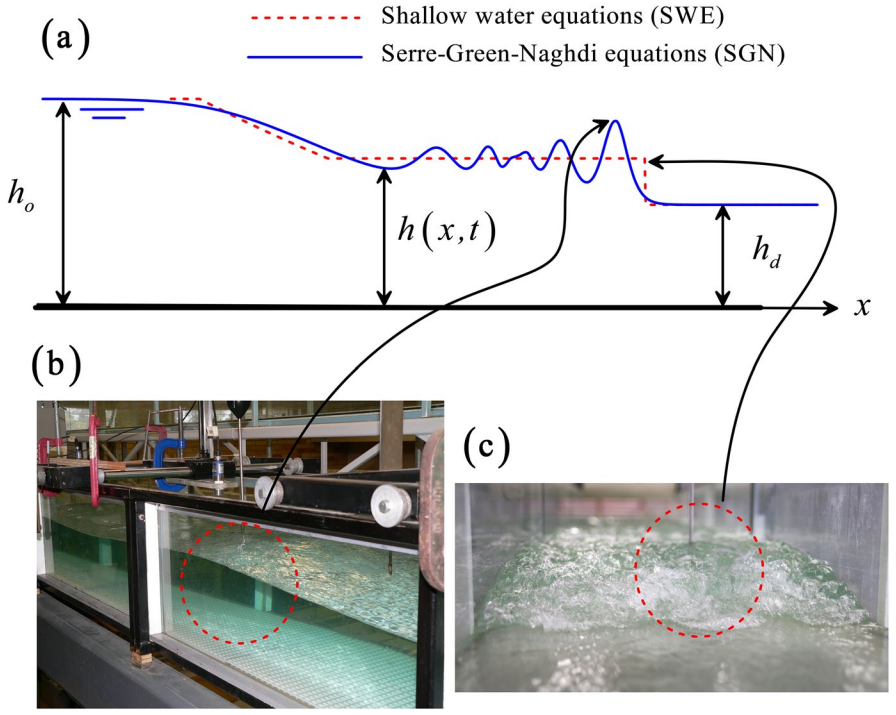

Fig. 1 Ideal dam break waves **a** dispersive (SGN) and dispersionless (SWE) solutions, **b** photograph of undular surge ($h_d/h \approx 0.75$) with first wave crest travelling from left to right, **c** photograph of breaking surge ($h_d/h \approx 0.4$) looking upstream (tests at hydraulic flume of University of Queensland)

For $r = h_d/h_o > 0.4$–0.55 the dam break surge is undular (Fig. 1b), a feature linked to the existence of vertical accelerations and non-hydrostatic pressures [14, 15]. This feature is well-known to be out of the capabilities of the SWE, but Boussinesq-type models are able to replicate such wave motion [16, 17], the accuracy of the solution depending of the terms retained while making an approximate depth-averaging process of the Euler equations [18]. Most river flood waves resulting from the collapse of a dam are long, and, thus, we limit this study to the frequent case. The Serre–Green–Naghdi (SGN) equations are especially well-suited, given that this is an extended (non-hydrostatic) system of SWE for long waves (weakly dispersive) preserving full non-linearity [19]. Simulations of dam break waves using the SGN equations do predict undular or dispersive surges and rarefactions influenced by vertical accelerations. One would be inclined to discard the SWE for $h_d/h_o > 0.4$–0.55 and simply solve the SGN. However, for $r = h_d/h_o < 0.4$–0.55, the undular surge front begins to break (Fig. 1c), and for low r values such as $r = 0.1$ the surge is fully broken without any appreciable undulation on the flow profile [14]. This broken surge is very well predicted using the SWE, given that the wave front is approximated in the mathematical model as a discontinuity resulting from the weak solution of the hyperbolic conservations laws [3]. On the other hand, the SGN equations are unable to mimic wave breaking, and become unreliable for $h_d/h_o < 0.4$–0.55 unless some method to induce the breaking is added. Thus, one would be inclined to discard the SGN equations for $r = h_d/h_o < 0.4$–0.55 and simply solve the SWE. The consequence of the above discussion is that neither the SWE nor the SGN can be used (as they are) to predict dam break waves for an arbitrary value of r.

We remark that both the SWE and the SGN equations use a "height-type" method for determining the position of the free surface based on the depth-averaged continuity equation, e.g., the flow depth h is a single-valued function of the space coordinate x. It means that both models lack the ability to reproduce the overturning shape of a breaking wave [20]. We refer to wave breaking in a depth-averaged framework as the ability (or lack of it) of a depth-averaged model to mimic wave breaking by transformation of a wave into a surge. In maritime hydraulics there exists a vast experience working with improved Boussinesq-type models with breaking capabilities (see review in [21]). Basically, three types of techniques are possible in the Boussinesq-type models to 'reproduce' wave breaking:

1. The first option is to incorporate additional terms to represent "rollers" in the free surface once the inception of wave breaking is reached [22]. Typical of this family of models is the need to define the roller flow model itself, and a criterion to decide when the additional roller-type terms in the governing equations are activated.
2. A second possibility is to add to the Boussinesq equations additional terms representing eddy-viscosity effects in the breaking portion of the wave [23, 24]. As before, one would have to define the mathematical form of these terms, and a logic condition to decide when these are switched on- and off- during the simulation.
3. The third option, and possibly the most used at this time, is to construct a hybrid model combining the SGN–SWE equations. The rationale of these models is as follows. Broken surges and their energy dissipation are well characterized by the shocks produced by the solution of the SWE [25], while long non-breaking waves are accurately described by the SGN equations [26]. Thus, the recipe consists in using the SGN equations as base flow model and switch locally to the SWE in those portions of the computational domain where wave breaking is detected [27]. Consequently, a criterion to define the onset of

wave breaking is necessary, often requiring case-dependent calibration of parameters [28].

It is then logical to use SGN–SWE hybrid models, given that a criterion for deciding when a wave is breaking is needed in any case, but no additional terms are involved into the governing equations. The criterion for activation of wave breaking is in fact not unique, and it is common practice in maritime hydraulics to use various simultaneously [28, 29]. Regretfully, most are based on parameters requiring calibration to the specific wave problem investigated. Given the vast amount of literature in maritime hydraulics, this research started at testing the various criteria offered in maritime hydraulics for the specific problem of dam-break waves in riverine applications. After this preliminary phase, the fundamental objectives of this research were to answer two fundamental questions relating to the modeling of undular and broken dam break waves:

1. Why the SGN equations do not mimic wave breaking? The SGN equations are a higher-order system of depth-averaged equations, which reduces to the SWE if the non-hydrostatic terms are dropped. Already discussed is the fact that the SWE predict shocks (broken surges) with great accuracy. As the SWE are embedded into the SGN equations, one would expect breaking ability of the latter system. Further, the SGN equations are a very good approximation to the Euler (2D) equations for long waves, and it is thus unfortunate that breaking waves cannot be explained, at least approximately, with the SGN equations. The answer to this question will be partially addressed considering higher-order terms into the depth-averaged non-hydrostatic equations.
2. Is it possible to use an acceleration-based wave breaking sensor in SGN–SWE hybrid models? As demonstrated with detailed 2D simulations by Peregrine et al. [20], a wave which is about to break experiences a large acceleration in the breaking front, several times larger than gravity. A condition for the generation of the free jet spilling from a breaking wave is that the fluid velocity exceeds the phase celerity. Obviously, a large acceleration is a precursor needed to reach these kinematic conditions. Thus, the acceleration on the free surface may be an index of wave breaking conditions [30]. However, this physical index appears to be not tested for wave breaking in hybrid SGN–SWE Boussinesq-type models. The answer to this question will be in part addressed considering a new wave breaking 'sensor' following Peregrine et al. [20].

We remark that the answers to the above two questions are only partially addressed in this work, given that these are very complex and wide. However, to our knowledge, this is the first work were these issues are investigated for dam break waves. These two objectives are systematically developed in the next sections using a set of higher-order Serre–Green–Naghdi type non-hydrostatic long-wave equations with ability to mimic wave breaking automatically, and a new acceleration-based wave breaking condition to its use in the standard Serre–Green–Naghdi equations, where wave breaking is not automatically accounted for.

Note that dam-break waves are basically long waves originating under shallow water conditions, and, therefore, short wave modeling, as typical from deep to intermediate water depths in the ocean environment, was excluded from this research. Thus, techniques for improving the linear frequency dispersion of the Serre–Green–Naghdi equations are not considered in ensuing developments. Emphasis of this research is on the non-linear aspects of Boussinesq-type models, which are dominant during wave breaking processes.

2 The Su–Gardner wave breaking equations

Before presenting the extended equations, the following introductory section presents the usual fully non-linear and weakly dispersive model, namely the Serre–Green–Naghdi equations. The equations and their development are well-known, but this information is summarised here for convenience. The new developments are presented thereafter as a generalisation of current tools.

2.1 First Picard iteration cycle

In this work Picard's iteration results are considered for the potential velocity components (u, w) in the Cartesian (x, z) directions, and fluid pressure p. The development is well-known [18, 31, 32], and only the main results are stated here for introductory purposes. With ψ the stream function and ϕ the potential function, the 1D unsteady potential flow obeys the Cauchy-Riemann conditions [33–35]

$$u = -\frac{\partial \phi}{\partial x} = -\frac{\partial \psi}{\partial z}, \quad w = -\frac{\partial \phi}{\partial z} = +\frac{\partial \psi}{\partial x}. \tag{1}$$

Iteration of the velocity components (u, w) starting with uniform flow ($u=q/h$; $w=0$) as initial guess produces the following kinematic field for water waves propagating over horizontal terrain [18, 32]

$$w = -U_x z, \tag{2}$$

$$u = U + U_{xx}\left(\frac{h^2}{6} - \frac{z^2}{2}\right), \tag{3}$$

where h is the water depth, $U=q/h$ the mean fluid velocity, $U_x=\partial U/\partial x$ and $U_{xx}=\partial^2 U/\partial x^2$. An identical result is obtained expanding in power series (u, w) [19, 36]. As demonstrated by Carter and Cienfuegos [36] Eqs. (2)–(3) are a good kinematic model for long waves. Equations (2)–(3) are the fully non-linear potential velocity components resulting from the 1st Picard iteration cycle. The pressure distribution p is determined inserting Eqs. (2)–(3) into the vertical Euler equation as [19, 37]

$$\frac{p}{\rho} = g(h-z) + \int_z^h \left(\frac{\partial w}{\partial t} + u\frac{\partial w}{\partial x} + w\frac{\partial w}{\partial z}\right) dz \approx g(h-z) + \left(U_x^2 - UU_{xx} - U_{xt}\right)\left(\frac{h^2 - z^2}{2}\right), \tag{4}$$

where $U_{xt}=\partial^2 U/\partial x \partial t$ and t is the time. We remark that Eq. (4) is only approximate: it was determined assuming $u \approx U$. To produce the Boussinesq-type equations, the vertically-integrated mass and momentum equations are considered here, namely [18, 19]

$$\frac{\partial h}{\partial t} + \frac{\partial}{\partial x}\int_0^h u \mathrm{d}z = 0, \tag{5}$$

$$\frac{\partial}{\partial t}\int_0^h u\mathrm{d}z + \frac{\partial}{\partial x}\int_0^h \left(u^2 + \frac{p}{\rho}\right)\mathrm{d}z = 0. \tag{6}$$

The integrals needed in Eqs. (5)–(6) are evaluated as follows [18, 37]

$$\int_0^h u\mathrm{d}z = Uh, \quad \int_0^h u^2\mathrm{d}z \approx U^2 h, \tag{7}$$

$$\int_0^h \frac{p}{\rho}\mathrm{d}z \approx g\frac{h^2}{2} + \left(U_x^2 - UU_{xx} - U_{xt}\right)\frac{h^3}{3}, \tag{8}$$

where the usual simplification $u \approx U$ is implicit [37]. Inserting Eqs. (7)–(8) into Eqs. (5)–(6) yields

$$\frac{\partial h}{\partial t} + \frac{\partial (Uh)}{\partial x} = 0, \tag{9}$$

$$\frac{\partial (Uh)}{\partial t} + \frac{\partial}{\partial x}\left[U^2 h + g\frac{h^2}{2} + \left(U_x^2 - UU_{xx} - U_{xt}\right)\frac{h^3}{3}\right] = 0. \tag{10}$$

Equations (9)–(10) are the well-known Serre–Green–Naghdi (SGN) equations for 1D water waves over horizontal terrain [37–40]. These equations are extensively used in maritime hydraulics [19, 23, 41, 42]; see review by Brocchini [21], but much less in river flow applications [43–46]. The steady-state version of the equations is frequently used in flow over channel structures [47–50]. The SGN equations are known to be an excellent approximation to the Euler equations for long waves, excluding wave breaking conditions, as demonstrated by Nadiga et al. [26] for undular bores propagating over obstacles and Viotti et al. [51] for the runup of long wave packets impinging on vertical walls. The purpose of this section was to show how Eqs. (9)–(10) were obtained from Eqs. (2)–(3) assuming $u(z) = U = q/h$. Note that Eqs. (9)–(10) are only valid for an ideal flat bottom topography, as they result from (2) and (3).

2.2 Velocity and pressure higher-order effects

The former section conveys a message: Eqs. (9)–(10) are only an approximate depth-averaged model, not only because of Eqs. (2)–(3) are approximations to the exact 2D velocity field, but, additionally, because the variation of u with z is fully overlooked once $u = U$ is set as part of the depth-averaging process. It is immediate to realise that the differential advection of momentum is not included, and that it may be important in waves near breaking. Equations (9)–(10) are alternatively determined in other works using a rigorous scaling analysis of dispersion and non-linearity (e.g. in [19]). However, the effect of the neglected higher-order terms while conducting the depth-averaging process seems to be unknown. The authors are unaware on any previous work evaluating the impact of the neglected terms in Boussinesq-type simulations. We reconsider in this section the potential velocity components (u, w) given by Eqs. (2)–(3), and will use

them to perform integrals without neglecting higher order terms while conducting the depth-averaging process resorting to Eqs. (5)–(6).

The exact vertical pressure distribution resulting from the 1st Picard iteration cycle is thus

$$\begin{aligned}\frac{p}{\rho} &= g(h-z)+\int_z^h\left(\frac{\partial w}{\partial t}+u\frac{\partial w}{\partial x}+w\frac{\partial w}{\partial z}\right)\mathrm{d}z\\ &= g(h-z)+\int_z^h\left[-U_{xt}z-UU_{xx}z-U_{xx}^2\left(\frac{h^2}{6}z-\frac{z^3}{2}\right)+U_x^2 z\right]\mathrm{d}z\\ &= g(h-z)+\left(U_x^2-UU_{xx}-U_{xt}\right)\left(\frac{h^2-z^2}{2}\right)-U_{xx}^2\left(\frac{z^4}{8}-\frac{h^2z^2}{12}-\frac{h^4}{24}\right).\end{aligned} \tag{11}$$

The exact momentum and pressure force integrals are then

$$\int_0^h u^2\mathrm{d}z=\int_0^h\left[U+U_{xx}\left(\frac{h^2}{6}-\frac{\eta^2}{2}\right)\right]^2\mathrm{d}z=U^2h+U_{xx}^2\frac{h^5}{45}, \tag{12}$$

$$\int_0^h\frac{p}{\rho}\mathrm{d}z=g\frac{h^2}{2}+\left(U_x^2-UU_{xx}-U_{xt}\right)\frac{h^3}{3}+U_{xx}^2\frac{2h^5}{45}. \tag{13}$$

Using Eqs. (12)–(13) the higher-order vertically-integrated x-momentum equation resulting from the 1st Picard iteration cycle is

$$\frac{\partial(Uh)}{\partial t}+\frac{\partial}{\partial x}\left[U^2h+\tfrac{1}{2}gh^2\right]+\frac{\partial}{\partial x}\left[\underbrace{\left(U_x^2-UU_{xx}-U_{xt}\right)\tfrac{1}{3}h^3}_{D}\right]+\frac{\partial}{\partial x}\left(\underbrace{U_{xx}^2\tfrac{1}{15}h^5}_{B}\right)=0. \tag{14}$$

Shallow Water Equations

Serre- Green-Naghdi Equations

Su-Gardner breaking Equations

In Eq. (14), two additional terms appeared summed to the x-momentum equation of the Shallow Water Equations. The first, denoted by D, is the usual dispersion term modeled by the Serre–Green–Naghdi equations, while the term B is of a higher-order. This term originated from the variation of u with z. It was originally obtained by Su and Gardner [38], but they neglected B as compared to D in the final form of their equations, arguing that it is a higher order term. It will be shown in the next sections that this higher-order term gives breaking ability to the equations. Given that the term B was discovered by Su and Gardner [38], we name the higher-order equations as the Su-Gardner breaking (SG-B) equations, in recognition of their pioneering work. Note that Eq. (14) is exact in the sense that Eqs. (2)–(3) were rigorously used to produce depth-averaged equations. However, Eq. (14) is still only an approximation to the Euler equations.

To be shown with the numerical simulations is the fact that B can be safely neglected as compared to D for non-breaking waves. But, for breaking waves, the term B can be of larger magnitude than D, and thus, cannot be neglected. Note that in a wave profile at the onset of breaking not all the undulations are under breaking conditions. That is, typically the front of a surge is breaking while the tailwater waves are undular. It seeds the idea that a wave motion may not be governed by identical scales locally, and in a portion of the wave B may be important as compared to D (at the breaking front), whereas, in the remaining portion of the flow profile, B is not important as compared to D (undular waves at the tailwater).

Equation (14) is based on Eqs. (2)–(3), which are approximate potential velocity components suitable for modeling long waves. These velocity components imply a local vertical acceleration based on the depth-averaged velocity U and mathematically given by $\partial w/\partial t = -(\partial^2 U/\partial x \partial t)z$. The modeled local acceleration is responsible of the term $-1/3(\partial^2 U/\partial x \partial t)h^3$ appearing in D, and thus, determining the linear frequency dispersion relation $h_o\omega^2/g = (kh_o)^2/[1 + 1/3(kh_o)^2]$ of both the SGN and SG-B equations, where the linear frequency is ω, k is the wave number and h_o the water depth. The dispersive behavior of a Boussinesq-type model is therefore dependent on the approximation used for the local vertical acceleration, and, therefore, the simplified theory pursued here produces a linear frequency dispersion relation valid for shallow flows, typically down $kh_o < 1.2$, [18]. Therefore, the higher-order term proportional to U_{xx} in Eq. (3) affects the non-linearity of the SG-B depth-averaged equations, and, thus, the behavior of the model at wave breaking conditions. Conducting additional Picard iteration cycles it would be possible to include higher-order corrections into the local acceleration $\partial w/\partial t$, and, therefore, improve the dispersive properties of the ensuing model. In Matsuno [9] higher-order equations are presented. In the current work we have used Eqs. (2)–(3) as the kinematic field to approximate the modeling of long waves, and, therefore, the higher-order term B appeared into the governing equations. This approximation is fully consistent from a mathematical standpoint with the Picard iteration technique. Alternatively to Picard iteration the SGN-type equations can be developed by expanding the potential function in power series [9]. From this development other terms of the same order in the scaling analysis emerge. These would appear also in the next Picard iteration cycle. In our approximate treatment of the problem we have retained the results of the full 1st Picard iteration cycle. In this work, therefore, we limit the development to shallow-water conditions, typical of dam break waves, thereby excluding the modeling of short waves.

2.3 Scaling analysis

The importance of the higher-order term B will be qualitatively discussed here based on a scaling analysis. Let us define the scaled variables (with hat)

$$\widehat{h} = \frac{h}{H}, \quad \widehat{x} = \frac{x}{L}, \quad \widehat{U} = \frac{U}{(gH)^{1/2}}, \quad \widehat{t} = \frac{t}{(H/g)^{1/2}}, \quad \varepsilon = \frac{H}{L}, \tag{15}$$

where the shallowness scaling parameter is $\varepsilon = H/L$, with H and L as representative vertical and horizontal length scales [52]. Our scaling analysis applies for long waves, as considered in the paper.

Using Eqs. (15) into Eq. (14) produces

$$\frac{\partial(Uh)}{\partial t}+\varepsilon\frac{\partial}{\partial x}\left(U^2h+\frac{1}{2}h^2\right)+\varepsilon^3\frac{\partial}{\partial x}\left[\left(U_x^2-UU_{xx}-U_{xt}\right)\frac{1}{3}h^3\right]+\varepsilon^5\frac{\partial}{\partial x}\left(U_{xx}^2\frac{1}{15}h^5\right)=0, \tag{16}$$

where hats are dropped for simplicity's sake. Let us compare the higher order of B (term proportional to ε^5) to D (term proportional to ε^3). If ε is sufficiently small, B can be neglected as compared to D. If ε is not small then B may play an important role in the wave motion.

Let us consider an undular surge with a breaking front (Fig. 2). At the surge front the breaking portion of the wave involves a roller of horizontal extension L and vertical thickness $H=H_2–H_1$ (Fig. 2a). At this wave, the scaling ε is a measure of the average free surface slope of the breaker, which is usually steep. Keeping this result in mind, it is expected that B will be important in breaking portions of a wave, where the average slope of the front increase (and hence ε), and unimportant elsewhere. This scaling reasoning will be verified below in the section with numerical simulations. It is accepted that a wave breaks in a depth-averaged framework if a threshold free surface slope $\partial h/\partial x$ is exceeded, among other conditions, as in [29]. Therefore, ε is a natural scaling to investigate waves at the onset of breaking.

The shallowness parameter $\varepsilon=H/L$ was used by Stoker [52], pp. 28–32] and Friedrichs [53] to derive by a perturbation method the hydrostatic Saint–Venant theory and Boussinesq equations. The specific choices of H and L are free, and, in our case, we related them to the conditions at a wave front. The shallowness parameter there can be considered a measure of the average free surface slope of a breaking wave. Note that in water wave modeling two parameters are usually selected for a scaling analysis of the equations of motion [19], the first, h_o/L, where h_o is the static water depth and L is the wave length, and the second is A/h_o, where A is the wave amplitude. The parameter h_o/L is used to visualize the importance of the dispersive features of the model, such that for long waves it is a very small quantity. In contrast, A/h_o is used as a measure of non-linearity, being important in waves close to breaking. In this paper the model equations considered are weakly dispersive given the restriction to the modelling of long waves. Thus, only non-linearity was accounted for in the higher-order correction term B. Therefore, the scaling analysis conducted here started by assuming long wave conditions thereby normalizing using the shallowness parameter, with our specific choices of the scales for interpretation of the local conditions at a wave front.

Note that the term B is essentially a non-hydrostatic higher-order term, which, however, is not affecting the linear dispersion relation of the SG-B equations. In [9] it is demonstrated that this term scales with $(h_o/L)^4$, as well as other dispersive terms that originated in the series expansion. Consideration of a second Picard iteration cycle would account for additional higher-order terms. Investigation of these terms could be a means of further improving the behavior at wave breaking conditions.

3 Hybrid modeling SGN–SWE

Prior to conducting a numerical solution of the SG-B equations, we elaborate below an hybrid SGN–SWE model. This will be used as reference to test how the new equations works in dam break wave problems.

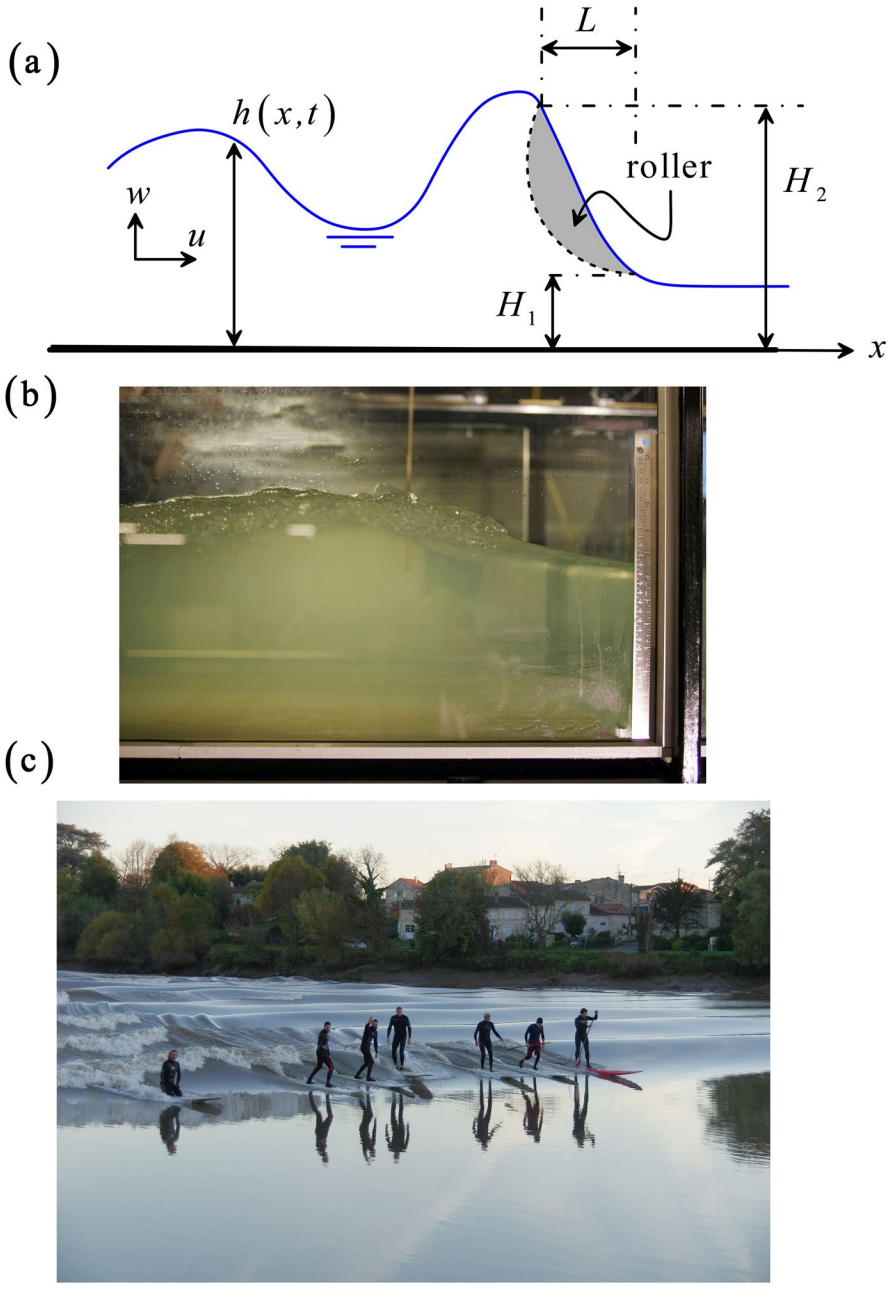

Fig. 2 Undular surge with breaking front **a** definition sketch **b** laboratory observation at the University of Queensland, with surge propagation from left to right and light breaking at the first wave crest **b** Dordogne River tidal bore at Luchey (France) on 30 October 2015—note the wave breaking on the left

3.1 Solution strategy

Consider the SG-B equations (Eqs. (9) and (14)) written in vector form as

$$\frac{\partial \mathbf{U}}{\partial t}+\frac{\partial \mathbf{F}}{\partial x}=\mathbf{S},$$
$$\mathbf{U}=\begin{pmatrix} h \\ Uh \end{pmatrix},\quad \mathbf{F}=\begin{pmatrix} Uh \\ U^2h+\frac{1}{2}gh^2 \end{pmatrix},\quad \mathbf{S}=-\frac{\partial}{\partial x}\begin{pmatrix} 0 \\ \frac{1}{3}\left(U_x^2-UU_{xx}-U_{xt}\right)h^3+\frac{1}{15}U_{xx}^2h^5 \end{pmatrix}, \tag{17}$$

where $\mathbf{U}$ is the vector of unknowns, $\mathbf{F}$ is the flux vector and $\mathbf{S}$ the source term. Dropping B, the SGN equations read

$$\frac{\partial \mathbf{U}}{\partial t}+\frac{\partial \mathbf{F}}{\partial x}=\mathbf{S},$$
$$\mathbf{U}=\begin{pmatrix} h \\ Uh \end{pmatrix},\quad \mathbf{F}=\begin{pmatrix} Uh \\ U^2h+\frac{1}{2}gh^2 \end{pmatrix},\quad \mathbf{S}=-\frac{\partial}{\partial x}\begin{pmatrix} 0 \\ \frac{1}{3}\left(U_x^2-UU_{xx}-U_{xt}\right)h^3 \end{pmatrix}. \tag{18}$$

An hybrid SGN–SWE model solves Eq. (18) in the whole computational domain. When breaking is detected, the dispersive term D is deactivated there and the SWE are solved in this portion of the wave profile, e.g.,

$$\frac{\partial \mathbf{U}}{\partial t}+\frac{\partial \mathbf{F}}{\partial x}=\mathbf{0},$$
$$\mathbf{U}=\begin{pmatrix} h \\ Uh \end{pmatrix},\quad \mathbf{F}=\begin{pmatrix} Uh \\ U^2h+\frac{1}{2}gh^2 \end{pmatrix}. \tag{19}$$

The hybrid application of Eqs. (18)–(19) requires determining a criterion for the onset of breaking in the depth-averaged framework.

3.2 Breaking conditions

Several conditions are used in the literature to decide if a portion of a wave profile is about to break in Boussinesq-type phase resolving simulations. Here we follow the detailed work by Kazolea et al. [29], who used a hybrid criteria summarized below. A first physical condition states that a wave breaks if the velocity of vertical displacement of the free surface exceeds a fraction γ of the long wave phase celerity [29]:

$$\frac{\partial h}{\partial t}\geq \gamma(gh)^{1/2}. \tag{20}$$

The parameter γ is not universal and ranges from 0.35 to 0.65, depending on the physical problem simulated. A second criterion is [29]

$$\left|\frac{\partial h}{\partial x}\right|\geq \tan\left(\phi_c\right), \tag{21}$$

which states that a wave begins to break once the local free surface slope exceeds a limiting inclination, with ϕ_c as the critical front angle. The value of ϕ_c is not universal, and

typically ranges from 14° to 33°, depending on the wave motion simulated. Further, once a roller is identified on a wave, its Froude number F may be defined as (Fig. 2):

$$\mathrm{F} = \left[\frac{1}{8}\left\{\left(2H_2/H_1+1\right)^2-1\right\}\right]^{1/2}, \tag{22}$$

by analogy with the hydraulic jump in translation [1, 52]. Despite the analogy between undular hydraulic jumps and undular surges, we do not pursue it here, following Montes [54]. Based on experimental observations, an undular surge breaks in the interval $1.5 \leq \mathrm{F} \leq 1.8$ [5, 55–58], such that outside its upper limit the wave is fully broken. Other works suggested a rather lower limit for the onset of undular surge breaking as $\mathrm{F_{lim}} = 1.2$ [59]. Therefore, a wave is broken only if the Froude number of the roller is above a limiting value $\mathrm{F_{lim}}$, e.g.,

$$\mathrm{F} \geq \mathrm{F_{lim}} \tag{23}$$

The three physical conditions stated, namely Eqs. (20), (21) and (23), must be applied to determine in which portion of the computational domain Eq. (19) is solved instead of Eq. (18). No calibration of the parameters was attempted in this work. In all our simulations, the default mean typical values are $\gamma = 0.5$, $\tan\phi_c = 0.5$ and $\mathrm{F_{lim}} = 1.3$. Other models for solving the SGN equations use artificial dissipation introduced into the numerical scheme to mimic breaking, instead of defining numerical rollers by resorting to the above physical conditions. Examples are the use of artificial viscosity by Mohapatra and Chaudhry [43] or the upwinding of U_x by Castro-Orgaz and Cantero-Chinchilla [46]. In this work we only consider hybrid models with wave breaking activated by physical conditions.

3.3 Roller definition

Before presenting the numerical scheme, common to Eqs. (18) and (19), the methodology to determine the portions of the computational domain governed by each equation is explained below following Kazolea et al. [29]:

1. The computational domain is divided into cells of width Δx; Eqs. (20) and (21) are checked in each cell. If either of the two conditions is satisfied, the cell is marked as breaking (dispersive terms switched-off).
2. Breaking cells are clustered to avoid the effects of dispersion acting between breaking cells which are very close. For this purpose, breaking cells at a distance equal or less than $4\Delta x$ are grouped into larger rollers. The stencil used to discretise dispersive terms has a width of $2\Delta x$ (second-order central finite differences), and we thus used a double length to group breaking cells and form rollers.
3. Once a roller is defined on the wave profile, its extension L and heights H_1 and H_2 (Fig. 2) are determined. If $\mathrm{F} < \mathrm{F_{lim}}$, the roller may not be physical, and their cells are considered again as non-breaking (dispersive terms switched-on back).
4. If $\mathrm{F} > \mathrm{F_{lim}}$, the length of the numerical roller is incremented to satisfy a minimum value determined as $L_{\min} = \Lambda(H_2 – H_1)$, with Λ typically ranging from 3 to 10. If Λ is too low the stability of the hybrid model is degenerated by the action of dispersion in non-breaking cells adjacent to rollers which are not strong enough to produce the breaking wave. In all our simulations we used $\Lambda = 10$. For comparison, experimental observations in station-

ary hydraulic jumps yielded $\Lambda = 4.4$ [60], although re-analysis of large scale breaking wave experiments, including tidal bores, suggests that Λ may be as high as 8 [28].

4 Numerical scheme

The numerical method is common to all models and consists in a finite-volume finite-difference scheme based on Castro-Orgaz and Cantero-Chinchilla [46]. A brief summary of the main aspects follows. An alternative form of Eq. (17) is obtained after some algebra by using the chain rule of calculus and the depth-averaged continuity equation,

$$\begin{aligned} &\frac{\partial \mathbf{W}}{\partial t} + \frac{\partial \mathbf{F}}{\partial x} = \mathbf{S_d}, \\ &\mathbf{W} = \begin{pmatrix} h \\ \sigma \end{pmatrix}, \quad \mathbf{F} = \begin{pmatrix} Uh \\ U^2 h + \frac{1}{2} g h^2 \end{pmatrix}, \quad \mathbf{S_d} = -\frac{\partial}{\partial x} \begin{pmatrix} 0 \\ C + B \end{pmatrix}, \end{aligned} \tag{24}$$

where

$$\sigma = Uh - \frac{1}{3} h^3 \frac{\partial^2 U}{\partial x^2} - h^2 \frac{\partial U}{\partial x} \frac{\partial h}{\partial x}, \tag{25}$$

$$C = \left[\left(\frac{\partial U}{\partial x} \right)^2 - U \frac{\partial^2 U}{\partial x^2} \right] \frac{1}{3} h^3, \tag{26}$$

$$B = \left(\frac{\partial^2 U}{\partial x^2} \right)^2 \frac{1}{15} h^5. \tag{27}$$

Equations (24) are the SG-B equations. Setting $B = 0$ one gets the SGN equations, whereas for $C = B = 0$ and $\sigma = Uh$ the SWE are regained. The system of Eqs. (24) is solved using a finite volume-finite difference method based on the MUSCL-Hancock scheme, which is second-order accurate in space and time. First, the source term $\mathbf{S_d}$ is neglected. The integral form of Eq. (24) then reads for the advection step [3]

$$\mathbf{W}_i^{\text{adv}} = \mathbf{W}_i^k - \frac{\Delta t}{\Delta x} \left(\mathbf{F}_{i+1/2} - \mathbf{F}_{i-1/2} \right). \tag{28}$$

Here Δt and Δx are the step sizes in the t and x axes, respectively, k refers to the time level, i is the cell index in the x-direction, and $\mathbf{F}_{i+1/2}$ is the numerical flux crossing the interface $i + 1/2$ between cells i and $i + 1$. A piecewise linear reconstruction is conducted within each cell, and the minmod limiter is applied to avoid spurious oscillations near discontinuities. The numerical flux is computed using the HLL approximate Riemann solver, and the Courant–Friedrichs–Lewy number CFL is limited below unity for stability of the explicit scheme. Once the result of Eq. (28) is available, the value obtained for the flow depth is final, but the auxiliary variable σ must be updated to include the effect of $\mathbf{S_d}$. A predictor–corrector finite-difference scheme to incorporate $\mathbf{S_d}$ in the solution is accomplished. The predictor step is

$$\sigma_i^p = \sigma_i^{\text{adv}} + \Delta t \left[-\frac{\partial (D+B)}{\partial x} \right]_i^{\text{adv}}, \tag{29}$$

where all the spatial derivatives are approximated using second-order central finite differences. Once σ_i^p is available at each cell, the non-hydrostatic velocity field is obtained by solving the Helmholtz-type Eq. (25), in the sense there is a non-vanishing source term in addition to the Laplacian of the depth-averaged velocity field, using central finite differences. The resulting system of equations is tridiagonal and easily invertible by resorting to the Thomas algorithm [61]. The corrector step is given by

$$\sigma_i^{k+1} = \sigma_i^{\text{adv}} + \Delta t \left[-\frac{\partial (D+B)}{\partial x} \right]_i^{p}, \tag{30}$$

which is adopted as the final step and involves identical operations to the predictor phase. The numerical accuracy of the solver for wave propagation was investigated using solitary wave propagation tests [45], where the numerical errors were analysed for variations in Δx and CFL. The model successfully passed the tests and produced accurate numerical propagations as compared to the analytical counterparts. The second-order central differences used to compute U_{xx} produce high frequency oscillations in the estimated B, that affected the stability of the model given the stringent test posed by the dam break problem. A five point moving average was applied to the computed U_{xx} prior to estimate B, thereby removing the numerical noise and resulting stable computations in all our simulations. For application of the SGN–SWE hybrid model the conditions given by Eqs. (20)–(21) are checked in each cell in discretized form after solving the SGN equations. Breaking portions on the free surface are then identified taking into account Eq. (23), and the SWE solved in those subdomains.

5 Performance of the Su–Gardner higher-order equations

5.1 Dam-break waves

The experimental data of Ozmen–Cagatay and Kocaman [62] at various normalized times $T = t(g/h_o)^{1/2}$ starting at abrupt gate removal are considered in Fig. 3 for a dam break wave test with $r = h_d/h_o = 0.1$ in a horizontal channel. Its upstream water depth is $h_o = 0.25$ m, the flume width is 0.3 m and the downstream water depth for this series is $h_d = 0.025$ m. Simulations are conducted using a fine mesh with CFL = 0.1 and $\Delta x = 0.01$ m in all the models tested to reduce truncation errors. However, computations were found to be stable for the typical values CFL = 0.4–0.5. Left panels of the figure contain the comparison of the SGN and SG-B equations. It can be observed that the SGN equations produce for all times a solitary-like dispersive surge, which is not attenuated. On the other hand, the SG-B equations produce wave breaking progressively. Note the large differences between both models at $T = 8.9$, where the surge predicted by the SG-B equations is fully broken. Although the shape of the wave predicted by the SG-B equations is not in precise agreement with experiments during the breaking process, the fact that this wave breaking is automatically conducted by the physical system of equations without any external condition to force it is considered a significant salient result. Previous depth-averaged models proposed in the literature use wave breaking sub-models (roller type terms, eddy-viscosity terms, local switch

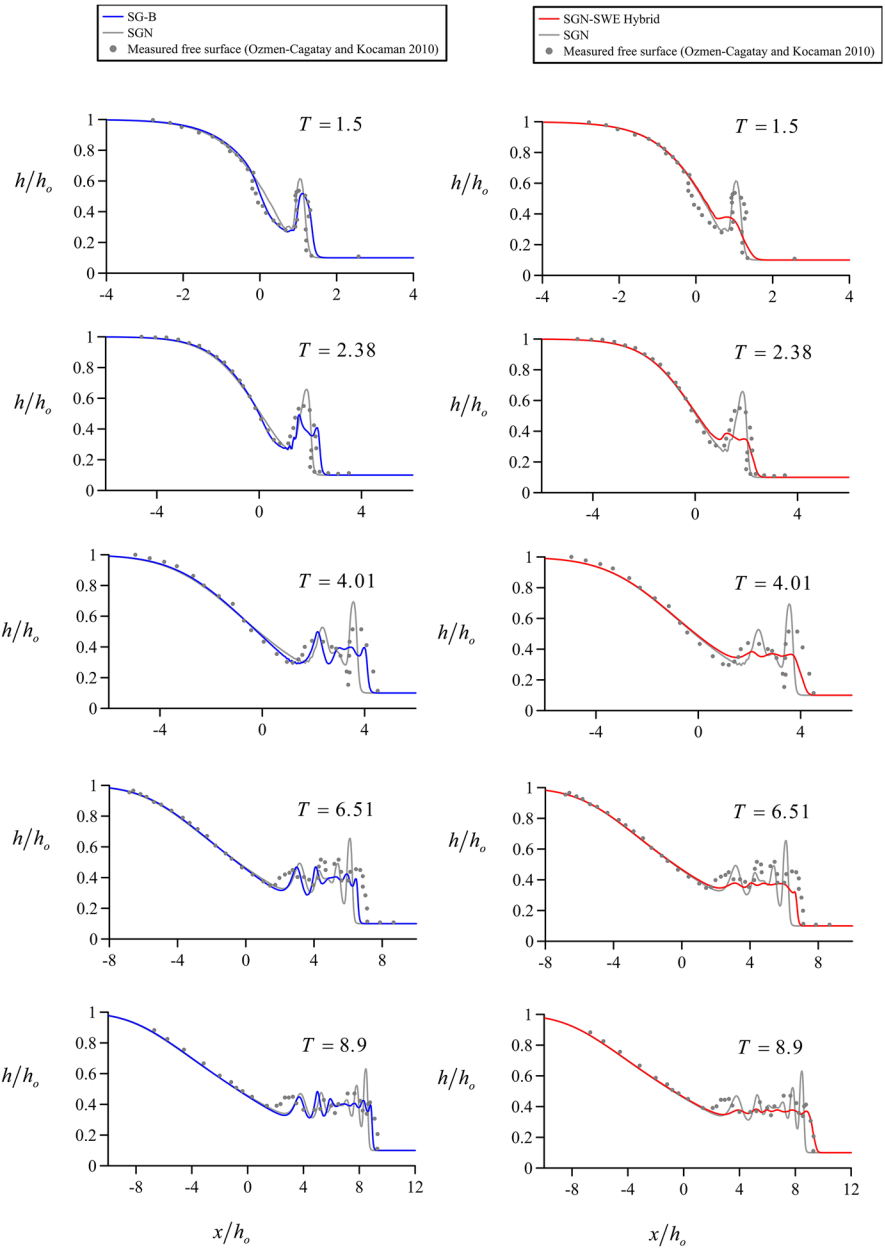

Fig. 3 Comparison of numerical simulations with experimental data (Ozmen-Cagatay and Kocaman [62]) for a dam break wave with $r=0.1$ using: the SG-B and SGN equations (Left panels) and the hybrid SGN–SWE and SGN equations (right panels)

to SWE) resorting to calibrated conditions to detect the onset of wave breaking. Note that the effect of B on the rarefaction wave is negligible. The rarefaction waves are accurately described by the SGN equations, as previously found by Castro-Orgaz and Chanson [63].

Given that the only difference between the simulations using the SGN and SG-B equations is that B is accounted for in the latter system, the important role of B in breaking waves is confirmed. The right panels contain a comparison of the SGN equations with the hybrid SGN–SWE model. During initiation of motion, wave breaking predicted by the hybrid model is excessive, whereas for $T=4.01$ onwards the predicted surge is similar to that determined with the SG-B equations. The interesting result is that the SG-B equations are able to produce a broken surge similar to that obtained with the hybrid SGN–SWE model without invoking any empirical parameter, whereas the latter model requires the use of a 3-parameter breaking module. The comparison is not aimed at discarding the use of the efficient hybrid SGN–SWE model, but rather, at opening alterative paths to implement wave breaking and exploring what is missing in the SGN to allow breaking capabilities. As a consequence of the present results, the variation of the velocity profile u with z shall be accounted for in the depth-averaged equations to allow wave breaking mimicking.

The experimental data of Ozmen-Cagatay and Kocaman [62] for a dam break wave test with $r=h_d/h_o=0.4$ is considered in Fig. 4, and a germane comparison between the various models is presented. In this test it is clearly observed (left panels) that the degree of "breaking" introduced by the SG-B is less than that observed in the experiments, as noted from the results at $T=8.9$. However, the hybrid SGN–SWE model is likewise underestimating the wave breaking, producing results again in close agreement with the SG-B equations.

Let us discuss the breaking ability of the SG-B equation system. Consider Fig. 5, where a snapshot of the undular surge simulated with the SGN equations for $r=0.1$ at $T=8.9$ is presented. For this (non-breaking) wave, the same figure contains a plot of the dispersion term D modeled in the SGN equations, as well as the breaking term B neglected. Upon comparing D with B it is noted that the neglected term is of higher magnitude than the modeled term! It means that B shall be retained in depth-averaged non-hydrostatic models for waves near breaking conditions. The former simulations confirmed that this term is responsible of wave breaking mimicking. Basically, for non-breaking waves D is the dominant term, and the solution of the SGN equations is nearly identical to that of the SG-B equations. As the wave progressively approaches breaking (reducing r in our case) the term B increases in magnitude and partially suppress the effect of D. For breaking waves, the sum $D+B$ tend to be a small quantity, thereby indicating that the solution of the SG-B system will be dominated by the underlaying SWE component embedded on them. It further confirms that in a breaker the scaling $\varepsilon=H/L$ is conceptually approached by the average slope of the breaking front, such that the effect of B progressively augments as the free surface slope increases.

Simulations of the Serre–Green–Naghdi equations do converge to analytical solutions during solitary wave propagation tests as both Δx and CFL are reduced. In the hybrid model SGN–SWE, however, the mesh cannot be refined without bounds, given that strong oscillations appears at the switching portion of the SGN and SWE sub-models. The SGN–SWE hybrid models are widely used in ocean research [21], but the generation of numerical instabilities during mesh refinement is a challenging difficulty precluding the establishment of fully grid-converged solutions, as discussed by Kazolea and Ricchuito [64]. In the case of the SG-B equations the discretization of the higher order term B was sensitive to significant refinement of the mesh down the minimum values $\Delta x=0.01$ m ($\Delta x/h_o=0.04$) and CFL$=0.1$ used. Further refinement of the mesh increased the high-frequency noise transmitted to the solution by the discrete central approximation to the derivative $\partial^2 U/\partial x^2$, forcing to introduce a stronger filter to the signal to grant stability of the model. Fully converged solutions are therefore difficult and open to further research.

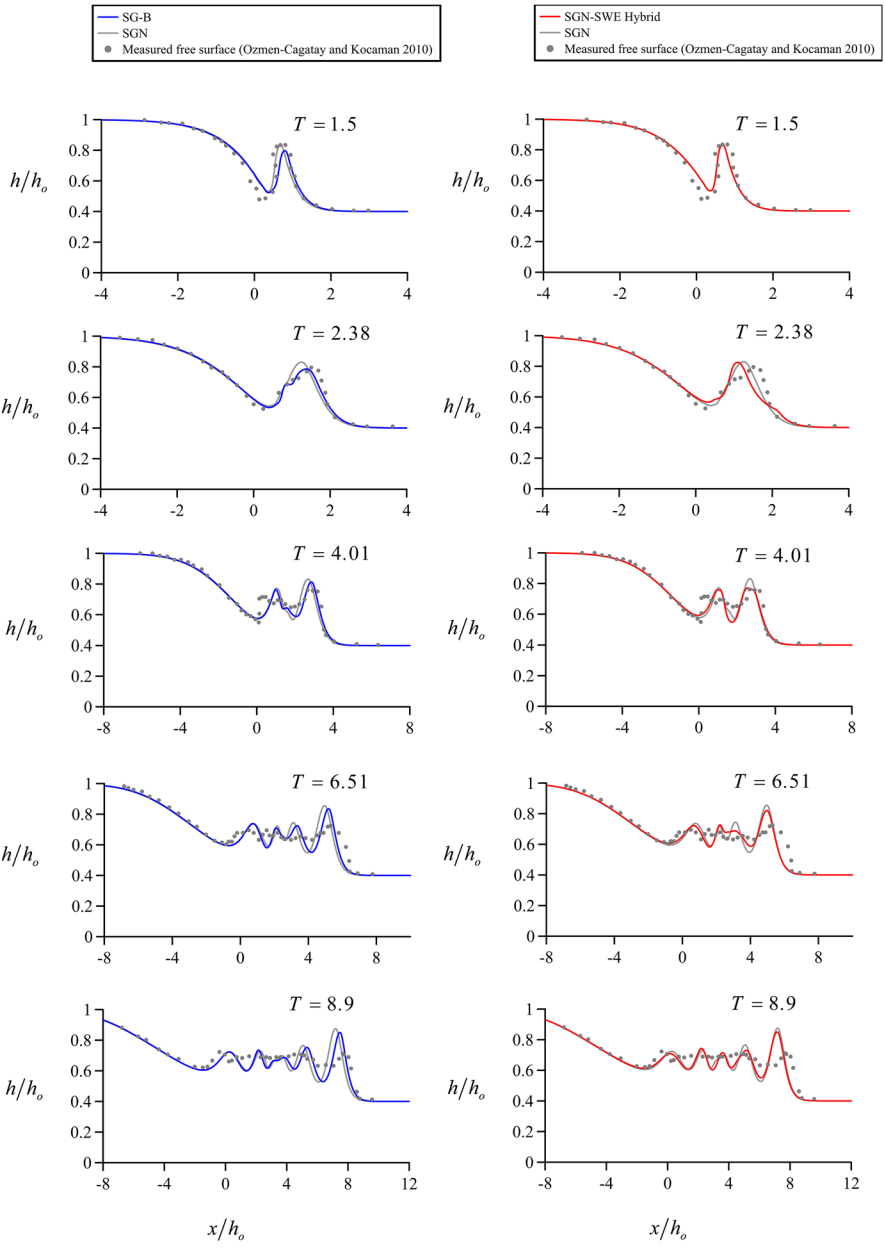

Fig. 4 Comparison of numerical simulations with experimental data (Ozmen-Cagatay and Kocaman [62]) for a dam break wave with $r=0.4$ using: the SG-B and SGN equations (left panels) and the hybrid SGN–SWE and SGN equations (right panels)

An obvious consequence of the breaking ability of the SG-B equations is that solitary wave solutions are not likely to exists for arbitrary values of F. Investigation of the solitary wave solutions of the SG-B equations is important because of it will highlight

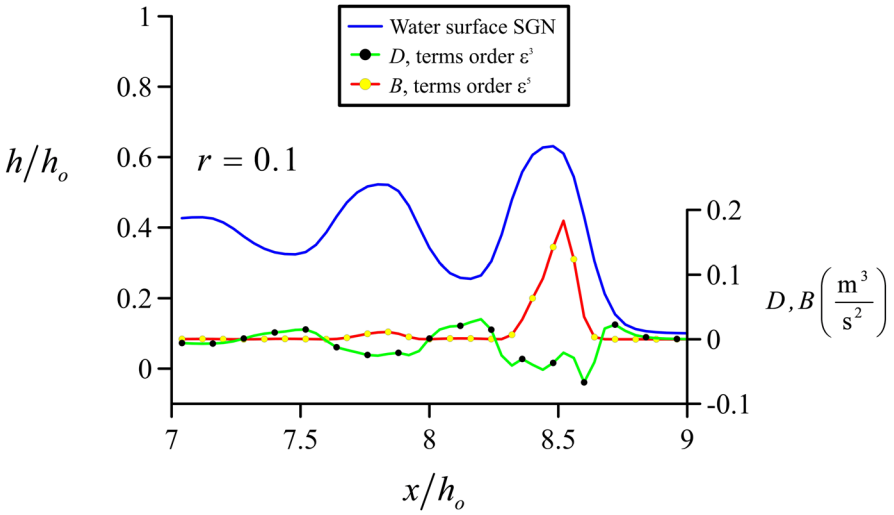

Fig. 5 Snapshoot of undular surge simulated with the SGN equations for $r=0.1$ at $T=8.9$ showing the dispersion term D modeled in the SGN equations and the neglected breaking term B

how the undular wave front of a dam break wave is expected to evolve in time under the action of the new wave breaking term. Solving the steady-state version of the SG-B system it was found that the upper bound for existence of solitary wave solutions is $F\approx 1.397$ ("Appendix"), which is in remarkable agreement with the experimental value for apparition of some breaking at the first crest of an undular surge $F=1.3$–1.4 [5, 55, 56]. Wave breaking starts to manifest progressively in the SG-B equations for $F>1.397$. A consequence of this finding is that waves of permanent shape with equilibrium between dispersion and non-linearity, e.g., solitary waves, cannot be expected for $F>1.397$. In this case the SG-B equations tend to transform any solitary-like wave into a shock ("Appendix").

Figure 6 shows a comparison of the SG-B equations with the experimental data by Stansby et al. [65] at several instants after removal of the gate from the flume. The upstream depth in the experiments was $h_o=0.1$ m and $r=0.45$. A lag of $t=0.04$ s was considered in the mathematical model to account for the gate opening time, given that the initiation of motion is instantaneous in the numerical flume. The comparison shows a fair reproduction of experiments by the numerical model, albeit with less intensity of breaking, as previously described in Fig. 4.

The solution of the SG-B at $T=15$ for $r=0.7$, 0.5 and 0.2 is presented in Fig. 7 for comparison purposes with the 2D simulations by Mohapatra et al. [66] using the Euler equations. Computations were again conducted using $\Delta x=0.01$ m and $CFL=0.1$. The rarefaction wave predicted by the SG-B equations is in excellent agreement with 2D results for all values of r. The undular surge agrees well with 2D results for $r=0.7$. For lower values the SG-B equations progressively produce wave breaking. Note that the amplitude of the leading wave is in good agreement with 2D results for the broken wave generated with $r=0.2$. The major discrepancy between 1D and 2D results is in the secondary waves, which are more damped in the 2D simulations.

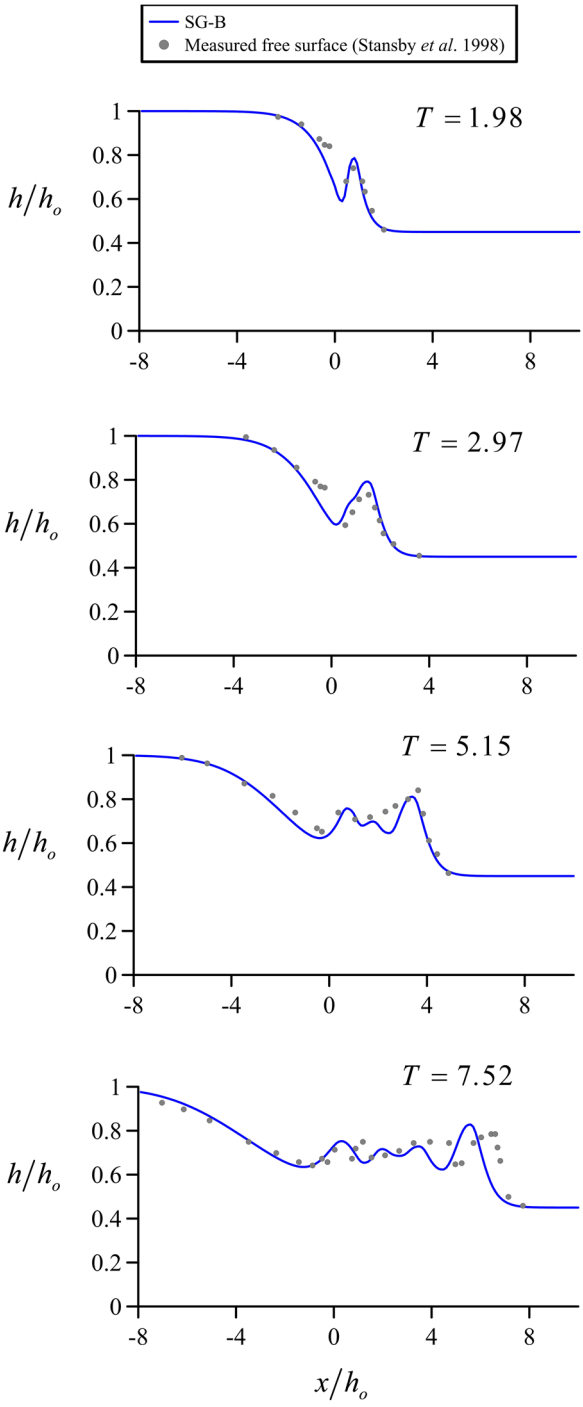

Fig. 6 Comparison of numerical simulations using the SG-B equations with experimental data (Stansby et al. [65]) for a dam break wave with $r = 0.45$

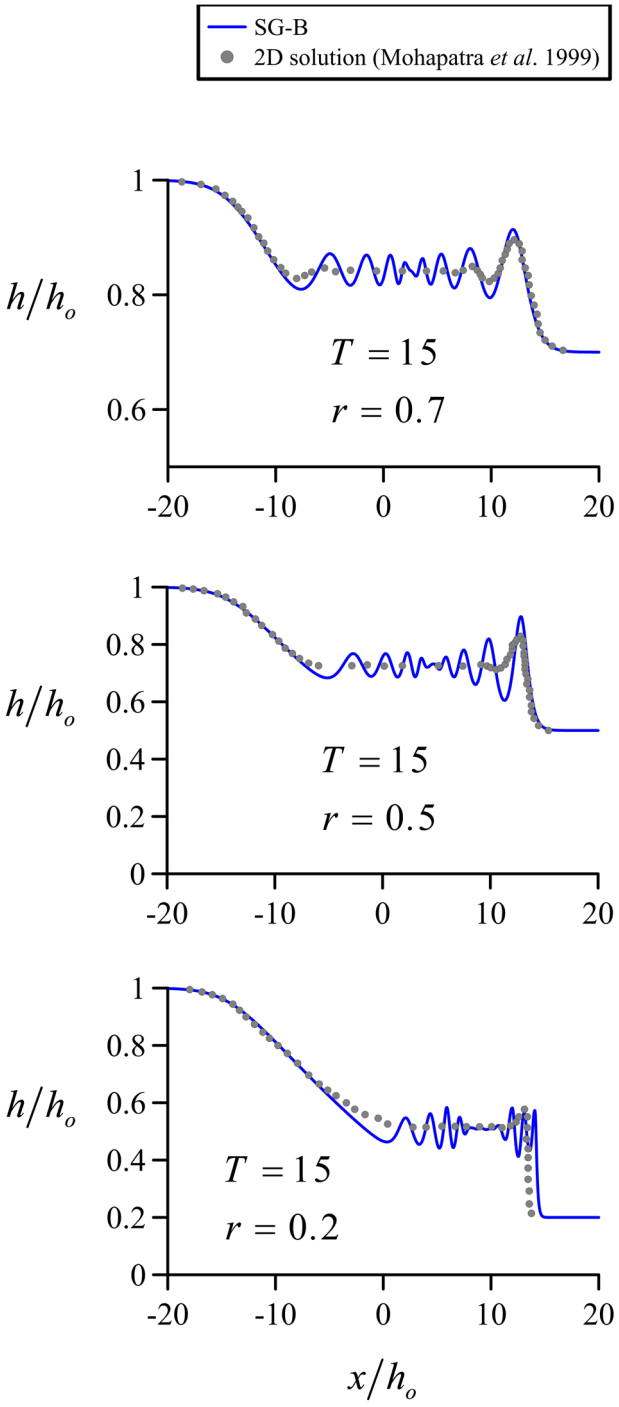

Fig. 7 Comparison of the SG-B equations at $T=15$ for $r=0.7$, 0.5 and 0.2 with the 2D simulations by Mohapatra et al. [66] solving the Euler equations

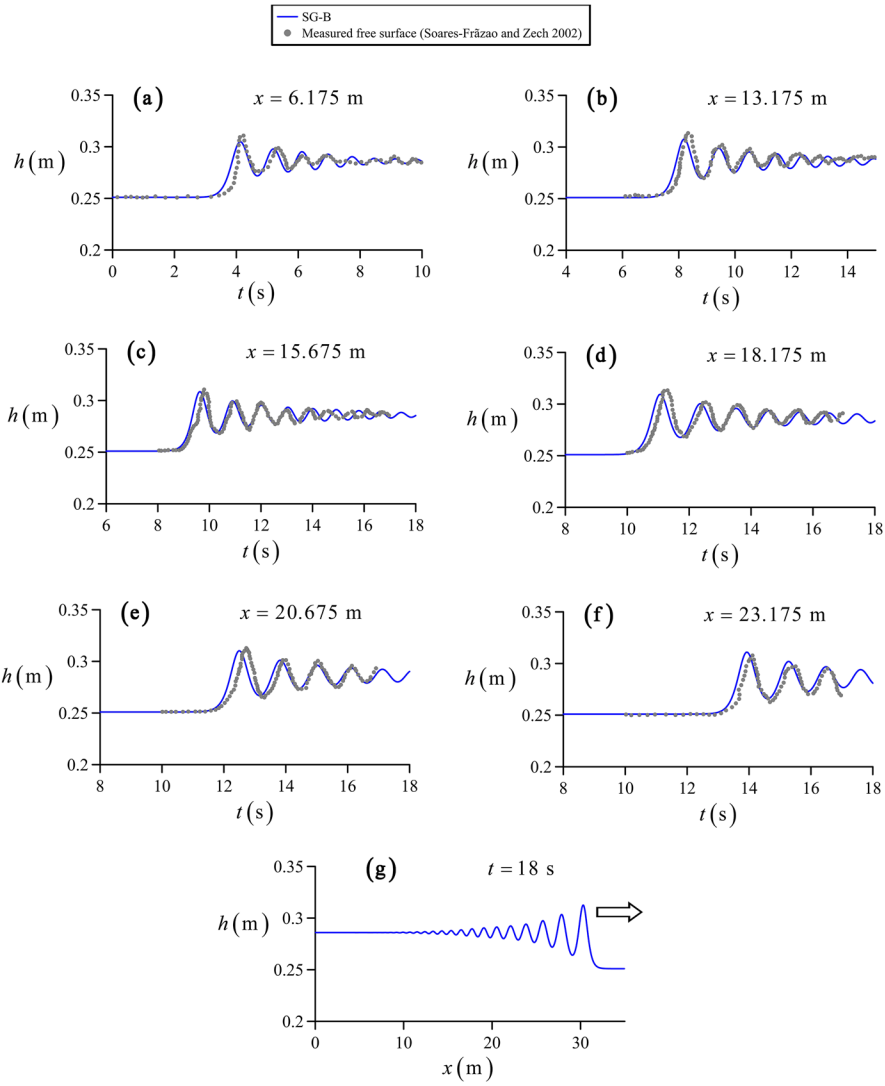

Fig. 8 **a–f** Comparison of the depth-hydrographs predicted by the SG-B equations at several positions with the experimentally measured Favre waves (F = 1.104) by Soares-Frazão and Zech [67], **g** computed free surface profile at $t = 18$ s

5.2 Undular Favre waves

The ability of the SG-B model to propagate undular bores was tested using the experiments on Favre waves generated in a laboratory flume after a fast partial gate opening [67]. Computations were conducted using $\Delta x = 0.025$ m and CFL = 0.1. Experiments reported there were conducted in a flume 1 m wide and 26.15 m long, with an initial water depth of 0.251 m. The evolution of the undular bore was measured using water level gauges positioned at several distances from the gate (see Fig. 8). The bore Froude number of these

experiments [Eq. (22)] is F = 1.104. Note that the comparison of the depth-hydrographs predicted by the SG-B equations at several positions with the experimentally measured Favre waves is generally good (Fig. 8), although the first experimental wave is a bit delayed as compared to simulations.

5.3 Undular tidal bore

Chanson [55] conducted experiments on undular tidal bores in a 0.5 m wide, 12 m long rectangular and horizontal flume. A radial gate at the tailwater portion of the flume ($x = 11.15$ m) was used to create the desired (initial) steady subcritical flow. A fast closing of a tainter gate close to and upstream of the radial gate produced an undular surge that propagated in the upstream direction. Depth-hydrographs were measured with acoustic displacement meters at several positions (see Fig. 9). A run for discharge $Q = 0.019$ m^3/s, $h_o = 0.191$ m (subcritical initial conditions) and F = 1.11 is considered in the figure, were computations using the SG-B equations are compared with observations. Computations were conducted using $\Delta x = 0.01$ m and CFL = 0.1. Gate closing was activated at $t = 27.4$ s

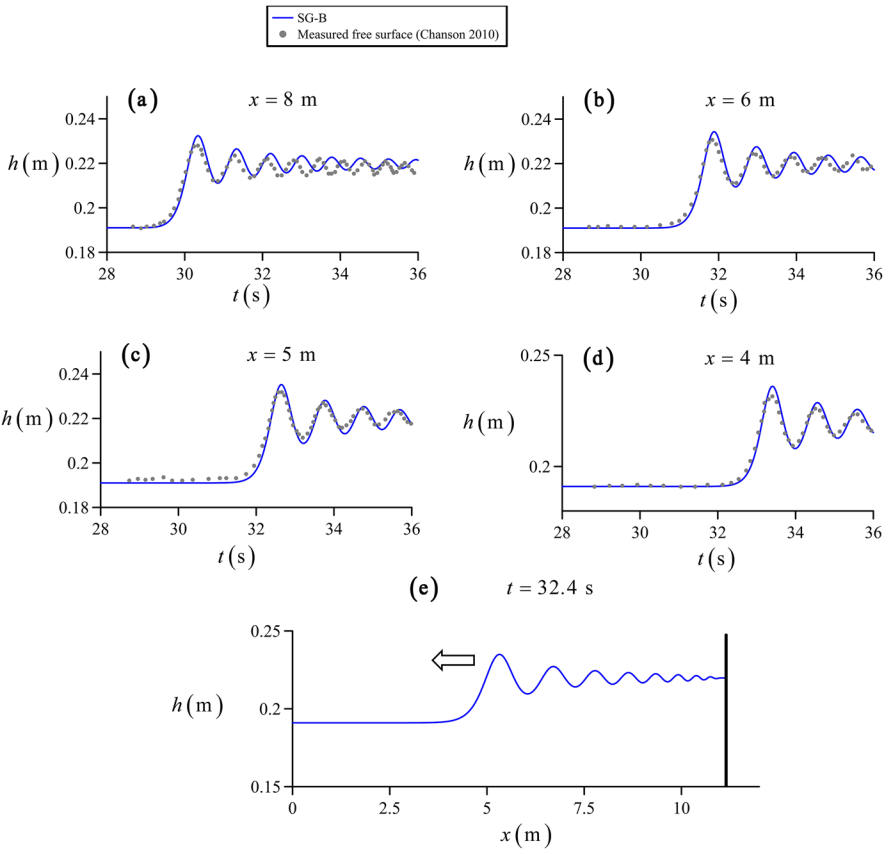

Fig. 9 **a**–**d** Comparison of the depth-hydrographs predicted by the SG-B equations at several positions with the experimentally measured tidal bore (F = 1.11) by Chanson [55], **e** computed free surface profile at $t = 32.4$ s

in the mathematical model. In general predictions are in fair agreement with observations, with the exception of the secondary waves at $x=8$ m (Fig. 9a), possibly due to the highly dispersive effects of these rather short waves.

6 Serre–Peregrine wave breaking sensor

Peregrine et al. [20] conducted 2D simulations of breaking waves and found that, at the onset of breaking, acceleration several times larger than gravity occurs on the face of the wave (Fig. 10a). The finding was recently confirmed in physical and 3D CFD numerical experiments [30, 68]. The free jet spilling from the breaking wave involves a fluid velocity on the free surface in excess of the phase celerity. The large acceleration is therefore a precursor of extreme kinematic conditions at the onset of breaking. Thus, we question now if the free surface acceleration is a viable index of wave breaking in Boussinesq-type models.

Consider Fig. 10b, where the normal acceleration component for a water particle on the free surface is sketched. For non-breaking conditions the particle must remain on the free surface. Therefore, breaking is initiated if the acceleration normal to the free surface a_n becomes negative, e.g.,

$$a_n = g\cos\theta + \frac{V_s^2}{R} \leq 0, \tag{31}$$

where θ is the free surface inclination, R the free surface radius of curvature, and V_s the particle velocity at the free surface. Equation (31) was originally stated by Serre [37] and discussed for steady hydraulic jumps. The particle velocity components at the free surface are from Eqs. (2)–(3)

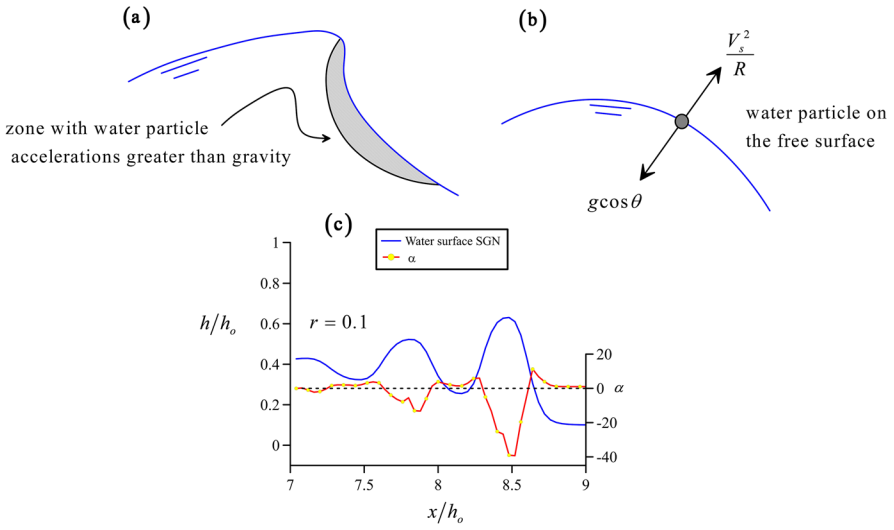

Fig. 10 Wave breaking **a** sketch of the onset of wave breaking (adapted from [20]), **b** determination of free surface acceleration **c** snapshot of undular surge simulated with the SGN equations for $r=0.1$ at $T=8.9$ showing the free surface acceleration sensor α

$$u_s = U - U_{xx}\frac{h^2}{3}, \qquad w_s = -U_x h. \tag{32}$$

Expressing θ and R as functions of h_x and h_{xx}, and normalizing using g, Eq. (31) produce the Serre–Peregrine acceleration-based breaking sensor α as

$$\alpha = 1 + \frac{u_s^2 + w_s^2}{g}\frac{h_{xx}}{1 + h_x^2} \leq 0, \tag{33}$$

where the breaking condition states that α becomes negative. The new proposed breaking sensor is physically-based and, as observed from Eq. (33), there is not a reference value to be calibrated for a specific wave motion. Consider Fig. 10c, where the snapshot of the undular surge simulated with the SGN equations for $r=0.1$ at $T=8.9$ is presented (see Fig. 5). For this (non-breaking) wave included in the same figure is a plot of the breaking sensor α, revealing its large (negative) values at the surge front. The behavior of the acceleration index seems to be well correlated to the breaking factor B. Therefore, it is of interest to investigate if α is a viable index for detecting wave breaking in Boussinesq models.

Figures 11 and 12 are analogue to Figs, 3 and 4 using in the hybrid SGN–SWE model Eq. (33) to activate breaking instead of Eqs. (20), (21) and (23). Comparing Fig. 11 with Fig. 3 and Fig. 12 with Fig. 4 it is appreciated that the results using the acceleration based breaking sensor [Eq. (33)] are very similar to those using the Eqs. (20), (21) and (23). Thus, the free surface acceleration is a possible index to detect wave breaking conditions, without involving calibration of a reference value for the α index.

The above wave breaking criterion is based upon ideal fluid considerations. In high-velocity turbulent water flow, the interactions with the atmosphere may yield to surface breaking and self-aeration [69, 70]. The conditions for the inception of surface breaking may be related to the turbulence in the water phase. It is basically recognized that air entrainment occurs when the tangential Reynolds stress acting next to the air–water interface is large enough to overcome the surface tension [70–72]. Ultimately, wave breaking in large geophysical systems such as tidal bores and tsunami surges is likely to be a combination of both ideal and turbulent fluid flow processes.

As early described by Peregrine et al. [20] a breaking wave involves a fluid velocity on the free surface in excess of the phase celerity. This breaking condition was extensively investigated by Barthelemy et al. [73] considering the local energy flux velocity at a breaking crest, and from their work a kinematic condition for the onset of wave breaking to test in our 1D numerical experiments is

$$\mathrm{F}_k = \frac{u_s}{c_w} \geq \mathrm{F}_{k,\mathrm{lim}} \approx 0.85, \tag{34}$$

where u_s is the horizontal velocity component at the wave crest, c_w is the water wave celerity and F_k a kinematic Froude number. Note that $\mathrm{F}_{k,\mathrm{lim}}$ is not unity. For implementation of this criterion in a Boussinesq-type model we follow Bacigaluppi et al. [74], thereby using Eq. (34) instead of Eq. (22) in the computational sequence of the hybrid SGN–SWE model. Therefore, a numerically-detected wave breaking is considered physical only if Eq. (34) is satisfied. Bacigaluppi et al. [74] presented computational results for their ocean research problems using $\mathrm{F}_{k,\mathrm{lim}}=1$ and $\mathrm{F}_{k,\mathrm{lim}}=0.75$. Here we consider the threshold value of 0.85 following Barthelemy et al. [73], which is rather close to an average of the values considered

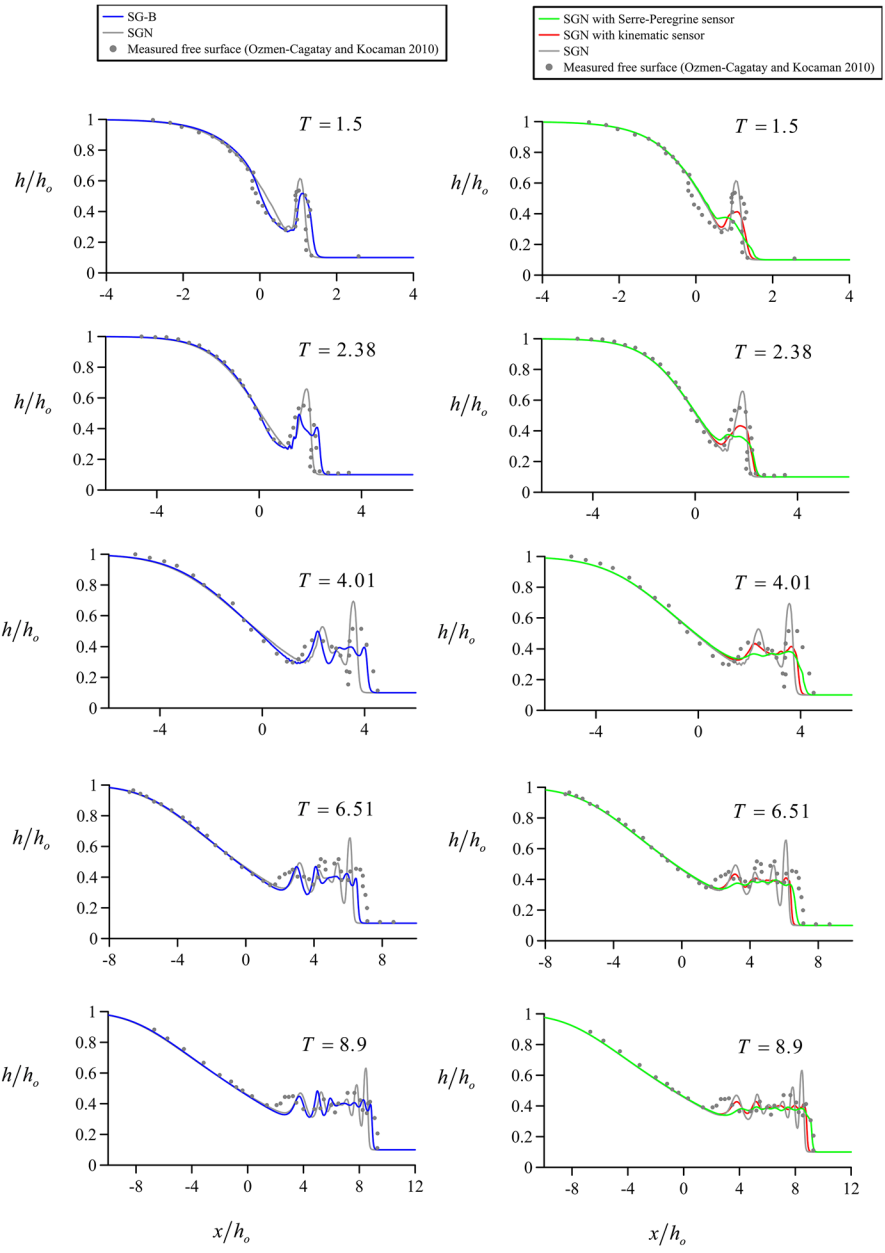

Fig. 11 Comparison of numerical simulations with experimental data (Ozmen-Cagatay and Kocaman [62]) for a dam break wave with $r=0.1$ using: the SG-B and SGN equations (left panels) and the hybrid SGN–SWE with Serre–Peregrine acceleration sensor, kinematic sensor and SGN equations (right panels)

by Bacigaluppi et al. [74]. For a given wave tracked, u_s is easily evaluated using the first of Eqs. (32) in a finite-difference form. However, an estimation of c_w is needed. Assuming that the wave crest is not deformed, its celerity is estimated from [74]

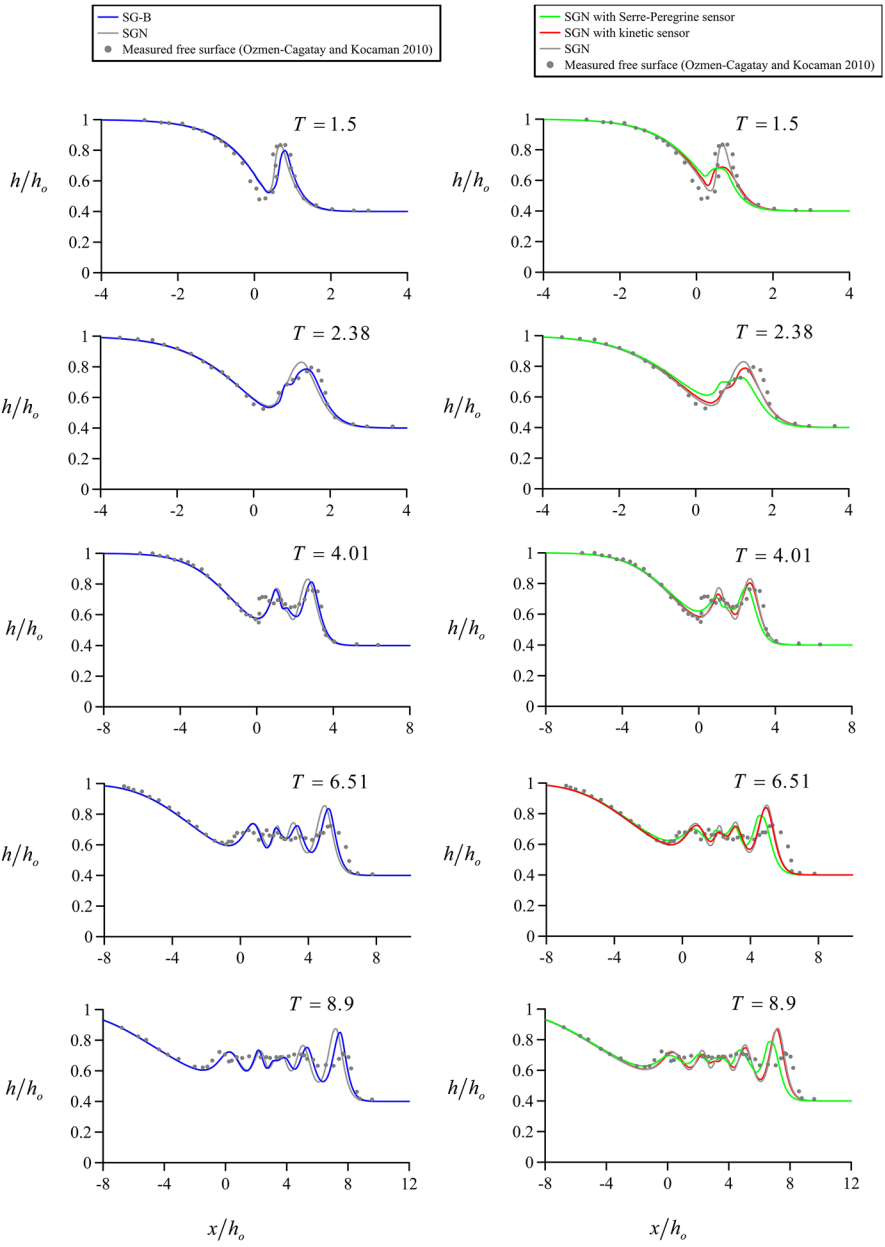

Fig. 12 Comparison of numerical simulations with experimental data (Ozmen-Cagatay and Kocaman [62]) for a dam break wave with $r=0.4$ using: the SG-B and SGN equations (left panels) and the hybrid SGN–SWE with Serre–Peregrine acceleration sensor, kinematic sensor and SGN equations (right panels)

$$c_w = \frac{\partial q}{\partial h}, \tag{35}$$

which is discretized using the flow conditions at the wave crest and trough as

$$c_w \approx \frac{q_{\text{crest}} - q_{\text{trough}}}{h_{\text{crest}} - h_{\text{trough}}}. \tag{36}$$

Simulations using the kinematic sensor given by Eq. (34) implemented in the hybrid SGN–SWE model (instead of the roller-based Eq. (22)) to physically accept a numerically-detected breaking wave, are inserted in the right panels of Figs. 11 and 12. As observed, simulations are very similar to those using the acceleration-based sensor and the SGN–SWE model with the rolled-based sensor. Thus, the kinematic sensor is an equally valid index to define the onset of wave breaking using Boussinesq-type models.

7 Transition from undular to breaking surge using different models

In this section we simulate dam break waves for different values of r and hence of F. We define F resorting to Eq. (22), using the flow depth of the undisturbed flow h_d as H_1, and the water depth behind the bore determined by the analytical solution of the SWE given by Stoker [52] as H_2. This water depth is a function of h_u solving the corresponding Riemann problem, thus $\text{F}=\text{F}(r=h_d/h_u)$. The analytical solution of the SWE is considered in the figure for reference.

Left panels of Fig. 13 compare the SGN, SWE and SG-B equations for F ranging from 1.71 to 3.13. The wave breaking ability of the SG-B equations is clearly observed. Note that the damping is progressive. At $\text{F}=1.88$ the wave is reasonably close to fully broken. Therefore, one may state that the transition from undular to broken bores using the SG-B occurs in the domain $\text{F}\approx 1.4$–1.9. This is fairly close to the experimental domain, which is $\text{F}=1.5$–1.8 [5, 55]. Right panels of Fig. 13 compare the SGN, SWE and hybrid SGN–SWE equations, using Eqs. (20)–(23) (red lines) and the Serre–Peregrine acceleration-based sensor (green lines). The hybrid models generally produce a faster transition to fully broken bores, as observed for example for $\text{F}=1.71$. Results of both hybrid models are again similar, with exception of a phase shift noted at $\text{F}=1.71$.

Finally, it should be noted that none of the models tested produce perfect results for all flow conditions. In fact, a critical outlook to the SG-B requires to stress that the introduction of breaking is rather slow and gradual. Consider a tidal bore measured by Leng and Chanson [56] in a 0.7 m wide, 19 m long rectangular and horizontal flume. A radial gate at the tailwater portion of the flume ($x=18.1$ m) was used to create initial steady subcritical flow. A fast closing of a tainter gate produced a surge that propagated in the upstream direction. A run for discharge $Q=0.101$ m^3/s, $h_o=0.172$ m (subcritical initial conditions) and $\text{F}=1.6$ is considered in Fig. 14, where it is observed that the surge is broken. For this Froude number one would not expect a fully broken surge from the SG-B equations, based on the results presented in Fig. 13. A simulation using the SG-B equations is compared with observations in the figure using $\Delta x=0.01$ m and $\text{CFL}=0.1$. For reference, the same computation was accomplished solving the SGN equations. Note by comparing the SG-B and SGN equations that the former system clearly produces breaking in the solution. In fact, the prediction of the first wave crest is reasonably good. Note that the experimental flow profile was obtained averaging data from many repetitions [56]. The maximum first wave crest elevation recorded during the repetitions is 0.33 m, which is rather close to the value predicted by the SG-B equations. In contrast, the SGN poorly predict the first wave crest. The main failure of the SG-B equations in this test is in the prediction of the

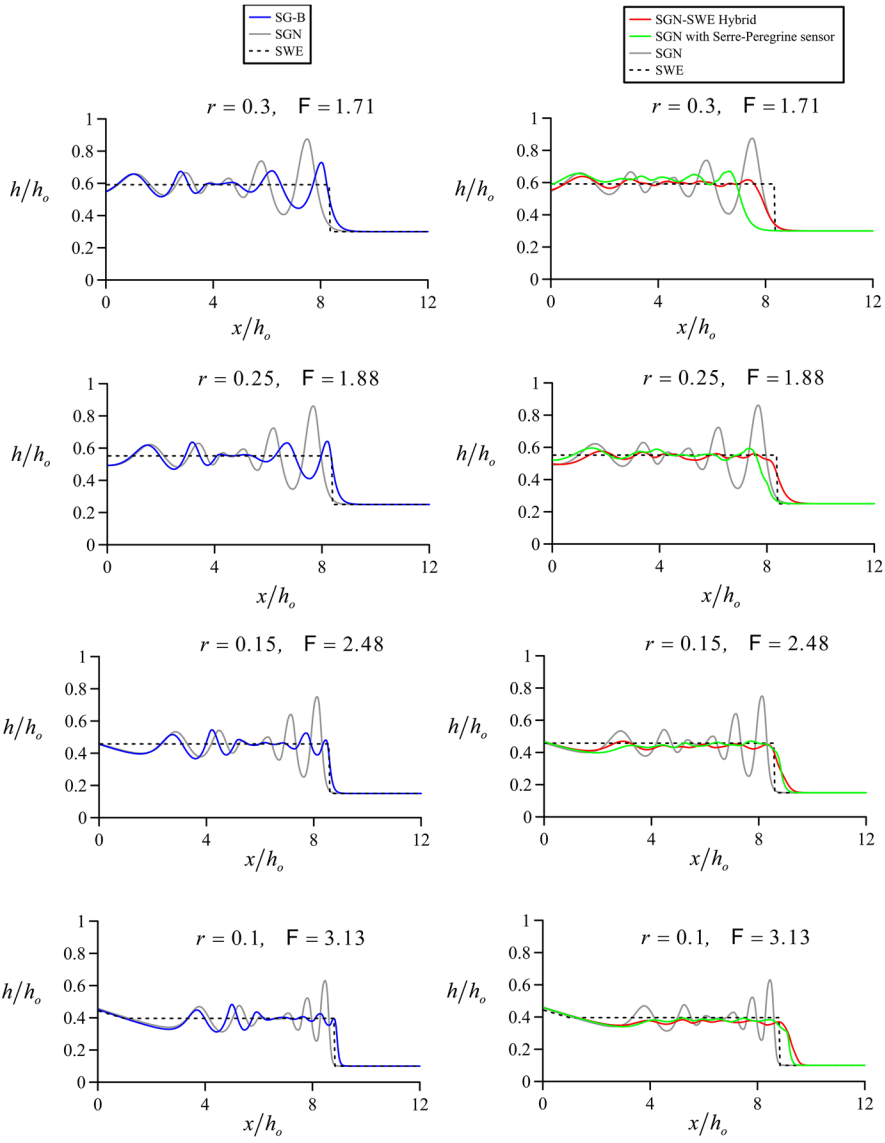

Fig. 13 Evolution of the wave breaking as function of r(F) using the various models tested (results displayed at $T=8.9$)

secondary waves, where the degree of breaking introduced is clearly below that indicated by experiments. However, it is clear as well that the SG-B equations produce a significant improvement as compared to the SGN equations. Therefore, the SG-B equations are able to produce a gradual transition from undular to broken bores, although the transition is rather slow. Given that the solution is accomplished based on ideal fluid flow computations, without resorting to any turbulent parameterization, it is logic to expect the deviations from experiments observed in Fig. 14. Another important case involving long wave

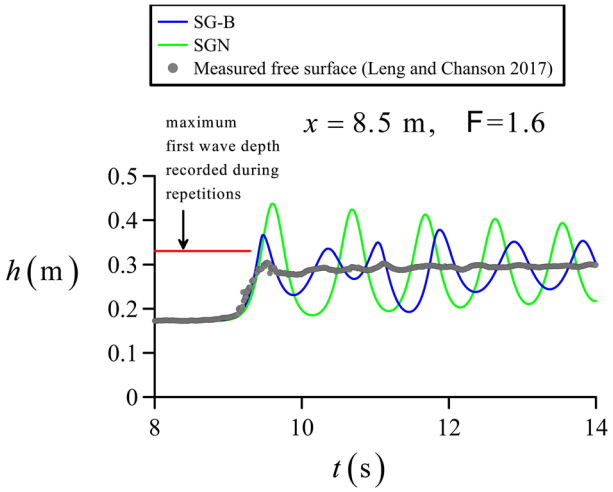

Fig. 14 Comparison of tidal bore predicted by SG-B and SGN equations with experiments (Leng and Chanson [56]); F = 1.6

non-hydrostatic flow modelling is the impact on a wall of a long-wave packet constructed using linear waves [51]. In most cases tested by Viotti et al. [51] the solution obtained by the SGN model is in good agreement with the full Euler equations. For a 3-wave packet of amplitude 15% of the initial water depth at rest h_o, the wave amplitude at the wall after impact was close to 82% of h_o, that is, close to the onset of wave breaking. Simulations conducted with the SGN and SG-B equations solvers produced in this research showed minor variations. This was expected, given that the simulation conducted is at the onset of wave breaking, and, as previously discussed, one of the deficiencies of the SG-B model is that breaking is very slowly introduced, such at the onset of breaking the effect of B is weak.

8 Conclusions

In this work the undular and broken surges originating from the dam break flows in a horizontal channel were investigated, and the following conclusions were obtained:

- A new set of depth-averaged non-hydrostatic equations was obtained rigorously taking into account the variation of u with z while conducting the vertical integration process. The result is an x-momentum equation containing a higher-order term, as given by Picard's iteration. The equations are called herein the Su-Gardner breaking (SG-B) equations. Numerical solution of the improved set of equations demonstrated that the new higher-order term acquires importance in breaking waves. As a result, the improved equations are able to represent the transition from undular to broken surges automatically without the need of any external forcing. For non-breaking waves the SG-B equations yields almost identical results to the Serre–Green–Naghdi (SGN) equations. For broken waves, SG-B equations generate similar results to those obtained with SGN–SWE hybrid models. The transition from undular to breaking bores in the SG-B model occurs in the interval F = 1.4–1.9, very close to the experimental observations F = 1.5–1.8. Although there is some difference, it should be noted that the breaking activation and transition process from undular to broken surge is fully analytical in the SG-B equations, being triggered by the governing

equations themselves. It makes the model free from calibration parameters, whereas the SGN–SWE hybrid models rely on breaking modules depending on the parameters $\tan(\phi_c)$, γ, and F_{lim}.

- A new wave breaking sensor for use in hybrid SGN–SWE models was developed based on the acceleration at the free surface. Numerical results demonstrated that the predictions using this single index are similar to those based on the 3-parameters $\tan(\phi_c)$, γ and F_{lim}. The Serre–Peregrine acceleration-based wave breaking index does not involve calibration parameters, making the approach simple for implementation.

The purpose of this research was exploring why the SGN equations do not break and the role of a new sensor for SGN–SWE hybrid models based on the free surface acceleration. Results demonstrated that the introduction of higher-order terms, originating from the variation of u with z into the SGN equations, confers to the system breaking mimicking ability. It seeds the idea that modeling the velocity profile is a key issue to produce improved Boussinesq models valid (continuously) for both breaking and non-breaking waves. Further research is needed to generalise our results to flows over uneven beds and sediment transport. It was additionally observed that the acceleration at the free surface may be a suitable index to apply hybrid SGN–SWE models, given the similar results to other criteria actually used.

Funding The funding was provided by Secretaría de Estado de Investigacion, Desarrollo e Innovacion (This work was supported by the research project CTM2017-85171- C2-1-R).

Appendix: Solitary wave solutions

An important non-hydrostatic free surface flow is the solitary wave. Such travelling wave of permanent form is only possible when a balance between non-linearity and dispersion is achieved. In this section the existence of solitary wave solutions for the higher-order SG-B model is investigated. A wave of permanent form is steady for an observed traveling on the wave. Thus, the steady version of Eq. (14) reads

$$M = \frac{1}{2}gh^2 + U^2h\left[1 + \frac{1}{3}\left(hh_{xx} - h_x^2\right) + \frac{1}{15}\left\{\left(hh_{xx}\right)^2 + 4h_x^4 - 4h_x^2hh_{xx}\right\}\right] = gh_o^2\left(\frac{1}{2} + F_o^2\right), \tag{37}$$

where M is the momentum function, $h_{xx} = d^2h/dx^2$, $h_x = dh/dx$ and (h_o, F_o) refers to the water depth and Froude number of the undisturbed supercritical current. Manipulation of Eq. (37) permits to write it in the form $a(h_{xx})^2 + bh_{xx} + c = 0$. Therefore, $h_{xx} = [-b + (b^2 - 4ac)^{1/2}]/(2a)$. This second-order ODE can be easily solved transforming it into a pair of first-order ODEs to determine the profiles of h and h_x. Before conducting numerical simulations it shall be noted that real solutions do not exists for $b^2 - 4ac < 0$, which settles an upper limit of F_o for existence of solitary waves. A 4th-order Runge–Kutta scheme was used to compute the solitary wave solution for defined values (h_o, F_o) at $x = 0$. The value of h_x was fixed by choice to 0.001 to deviate the flow from uniform flow conditions. For a solitary wave

$$F_o = \left(1 + \frac{H}{h_o}\right)^{1/2}, \tag{38}$$

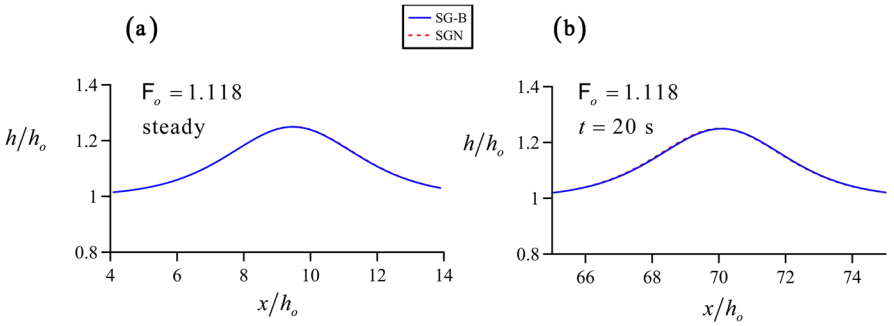

Fig. 15 Solitary wave for $F_o = 1.118$ ($H/h_o = 0.2$). **a** steady flow computations and **b** unsteady flow computations

where H is the maximum wave elevation (solitary wave crest) above the undisturbed depth h_o. Figure 15a contains the computed free surface profile for $F_o = 1.118$ ($H/h_o = 0.2$), which is close to those conditions used for the Favre waves simulated in Fig. 8. The numerical solution of the SG-B equations is compared there with the analytical solution of the SGN equations [18, 36]. It is the solution of the reduced equation [18, 75]

$$M = \frac{1}{2}gh^2 + U^2h\left[1 + \frac{1}{3}\left(hh_{xx} - h_x^2\right)\right] = gh_o^2\left(\frac{1}{2} + F_o^2\right), \tag{39}$$

which is obviously obtained from Eq. (37) neglecting the contribution of B. It can be verified comparing both solutions that for this case the effect of B is negligible. By numerical experimentation it was determined that solitary wave solutions ceased to exist at $F_o \approx 1.397$ ($H/h_o = 0.951$), given that $b^2 – 4ac < 0$ for higher values. Breaking of undular surges is often activated in Boussinesq models by checking the value of H/h_o at the surge front. The accepted approximate threshold condition for breaking in the SGN equations is $H/h_o = 0.8$ [27], resulting $F_o = 1.341$, which is rather close to the value obtained using our generalized SG-B equations. For $F_o > 1.397$ the SG-B will introduce breaking in the solution.

Now, let us check that the numerical solution of Eqs. (17) produces a travelling wave of permanent form. The procedure was as follows. The solitary wave analytical solution of the Serre–Green–Naghdi equations was set as an initial condition in the SG-B model, with the crest located at $x = 0$ for $t = 0$. The previous wave with $H/h_o = 0.2$ is considered. Obviously, this is not exactly the solitary wave solution of the SG-B model. When the numerical model is run the wave will evolve in time, producing imperceptible changes given the weak effect of B. Figure 15b shows the numerical solution of the SG-B equations at $t = 20$ s, and the analytical solution of the SGN equations. Note that differences are imperceptible. The numerical model produces a stable wave of permanent form, which is the solitary wave solution of the SG-B equations. Now, let us check the breaking ability of the SG-B equations. Following the same procedure, a solitary wave of $H/h_o = 1.5$ ($F_o = 1.581$) was routed and the results displayed at $t = 5$ s in Fig. 16. As expected, this value is above the previously detected threshold of breaking, and the numerical simulation transform the input solitary wave into a wave with a significantly reduced maximum height and steeper wave front, both features clearly resembling the wave breaking mimicking implicit in the SWE. For illustrative purposes the same simulation was conducted using the SWE, thereby transforming the solitary wave into a triangular wave with a shock front. The hybridised

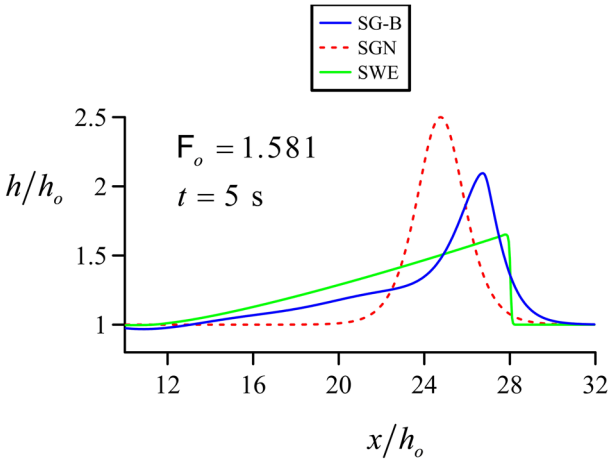

Fig. 16 Routing of a solitary wave of $F_o = 1.581$ ($H/h_o = 1.5$): comparison of the SWE and SG-B equations

character of the SG-B equations between the SGN and SWE is beautifully observed in this comparison.

References

1. Chanson H (2004) The hydraulics of open channel flows: an introduction. Butterworth-Heinemann, Oxford
2. Barré de Saint-Venant AJC (1871) Théorie du mouvement non permanent des eaux, avec application aux crues des riviéres et à l'introduction des marées dans leur lit. Comptes Rendus des séances de l'Académie des Sciences 73:147–154
3. Toro EF (2001) Shock-capturing methods for free-surface shallow flows. Wiley, Singapore
4. Jain SC (2001) Open channel flow. Wiley, New York
5. Chanson H (2011) Tidal bores, aegir, eagre, mascaret, pororoca: theory and observations. World Scientific, Singapore (ISBN 978-981-4335-41-6/981-4335-41-X)
6. Bonneton P, Chazel F, Lannes D, Marche F, Tissier M (2011) A splitting approach for the fully nonlinear and weakly dispersive Green-Naghdi model. J Comput Phys 230:1479–1498
7. Antunes do Carmo JS (2013) Boussinesq and Serre type models with improved linear dispersion characteristics: applications. J Hydraul Res 51:719–727
8. Lannes D, Marche F (2015) A new class of fully nonlinear and weakly dispersive Green-Naghdi models for efficient 2D simulations. J Comput Phys 282:238–268
9. Matsuno Y (2015) Hamiltonian formulation of the extended Green-Naghdi equations. Physica D 301–302:1–7
10. Clamond D, Dutykh D, Mitsotakis D (2017) Conservative modified Serre–Green–Naghdi equations with improved dispersion characteristics. Commun Non-linear Sci 45:245–257
11. Antunes do Carmo JS, Ferreira JA, Pinto L, Romanazzi G (2018) An improved Serre model: efficient simulation and comparative evaluation. Appl Math Model 56:404–423
12. Antunes do Carmo JS, Ferreira JA, Pinto L (2019) On the accurate simulation of nearshore and dam break problems involving dispersive breaking waves. Wave Motion 85:125–143
13. Christos E, Papoutsellis ML, Yates BS, Benoit M (2019) Modelling of depth-induced wave breaking in a fully nonlinear free-surface potential flow model. Coast Eng 154:103579
14. Nakagawa H, Nakamura S, Ichihashi K (1969) Generation and development of a hydraulic bore due to the breaking of a dam. Bull Disas Prev Inst Kyoto Univ 19(154):1–17
15. Betamio de Almeida A, Bento Franco A (1994) Modeling of dam-break flow. In: Computer modelling of free surface and pressurized flows, Nato Science Series E, Springer, Berlin, pp 343–373
16. Peregrine DH (1966) Calculations of the development of an undular bore. J Fluid Mech 25(2):321–330
17. Peregrine DH (1967) Long waves on a beach. J Fluid Mech 27(5):815–827

18. Castro-Orgaz O, Hager WH (2017) Non-hydrostatic free surface flows. In: Advances in geophysical and environmental mechanics and mathematics. Springer, Berlin. https://doi.org/10.1007/978-3-319-47971-2
19. Barthélemy E (2004) Nonlinear shallow water theories for coastal waters. Surv Geophys 25(3):315–337
20. Peregrine DH, Cokelet ED, Mciver P (1980) The fluid mechanics of waves approaching breaking. Coast Eng Proc S1(17):31
21. Brocchini M (2013) A reasoned overview on Boussinesq-type models: the interplay between physics, mathematics and numerics. Proc R Soc A 469:20130496
22. Madsen PA, Sorensen OR (1997) Surf zone dynamics simulated by a Boussinesq type model. Part I. Model description and cross-shore motion of regular waves. Coast Eng 32(4):255–287
23. Cienfuegos R, Barthélemy E, Bonneton P (2006) A fourth-order compact finite volume scheme for fully nonlinear and weakly dispersive Boussinesq-type equations. Part I: Model development and analysis. Int J Num Meth Fluids 51(11):1217–1253
24. Mignot E, Cienfuegos R (2009) On the application of a Boussinesq model to river flows including shocks. Coast Eng 56(1):23–31
25. Brocchini M, Dodd N (2008) Nonlinear shallow water equation modeling for coastal engineering. J Waterway Port Coast Ocean Eng 134(2):104–120
26. Nadiga BT, Margolin LG, Smolarkiewicz PK (1996) Different approximations of shallow fluid flow over an obstacle. Phys Fluids 8(8):2066–2077
27. Tonelli M, Petti M (2009) Hybrid finite volume—finite difference scheme for 2DH improved Boussinesq equations. Coast Eng 56(5–6):609–620
28. Lubin P, Chanson H (2017) Are breaking waves, bores, surges and jumps the same flow? Environ Fluid Mech 17(1):47–77. https://doi.org/10.1007/s10652-016-9475-y
29. Kazolea M, Delis AI, Synolakis CE (2014) Numerical treatment of wave breaking on unstructured finite volume approximations for extended Boussinesq-type equations. J Comput Phys 271:281–305
30. Lubin P, Kimmoun O, Veron F, Glockner S (2019) Discussion on instabilities in breaking waves: vortices, air-entrainment and droplet generation. Eur J Mech/B Fluids 73:144–156. https://doi.org/10.1016/j.euromechflu.2018.05.006
31. Matthew GD (1991) Higher order one-dimensional equations of potential flow in open channels. Proc ICE 91(3):187–201
32. Castro-Orgaz O, Hager WH (2014) 1D modelling of curvilinear free surface flow: generalized Matthew theory. J Hydraul Res 52(1):14–23
33. Rouse H (1938) Fluid mechanics for hydraulic engineers. McGraw-Hill, New York
34. Vallentine HR (1969) Applied hydrodynamics. Butterworths, London
35. Montes JS (1998) Hydraulics of open channel flow. ASCE Press, Reston VA
36. Carter JD, Cienfuegos R (2011) The kinematics and stability of solitary and cnoidal wave solutions of the Serre equations. Eur J Mech B/Fluids 30(3):259–268
37. Serre F (1953) Contribution à l'étude des écoulements permanents et variables dans les canaux. La Houille Blanche 8(6–7):374–388 (8(12), 830–887)
38. Su CH, Gardner CS (1969) KDV equation and generalizations Part III Derivation of Korteweg-de Vries equation and Burgers equation. J Math Phys 10(3):536–539
39. Green AE, Naghdi PM (1976) Directed fluid sheets. Proc R Soc Lond A 347:447–473
40. Green AE, Naghdi PM (1976) A derivation of equations for wave propagation in water of variable depth. J Fluid Mech 78:237–246
41. Dias F, Milewski P (2010) On the fully non-linear shallow-water generalized Serre equations. Phys Lett A 374(8):1049–1053
42. Tissier M, Bonneton P, Marche F, Lannes D (2012) A new approach to handle wave breaking in fully nonlinear Boussinesq models. Coast Eng 67:54–66
43. Mohapatra PK, Chaudhry MH (2004) Numerical solution of Boussinesq equations to simulate dam-break flows. J Hydraulic Eng 130(2):156–159
44. Kim D-H, Lynett PJ (2011) Dispersive and nonhydrostatic pressure effects at the front of surge. J Hydraulic Eng 137(7):754–765
45. Cantero-Chinchilla FN, Castro-Orgaz O, Dey S, Ayuso JL (2016) Nonhydrostatic dam break flows I: physical equations and numerical schemes. J Hydraulic Eng (ASCE) 142(12):04016068
46. Castro-Orgaz O, Cantero-Chinchilla FN (2020) Non-linear shallow water flow modelling over topography with depth-averaged potential equations. Environ Fluid Mech 20(2):261–291
47. Castro-Orgaz O, Hager WH (2009) Curved streamline transitional flow from mild to steep slopes. J Hydraulic Res 47(5):574–584
48. Castro-Orgaz O (2010) Approximate modeling of 2D curvilinear open channel flows. J Hydraulic Res 48(2):213–224
49. Castro-Orgaz O (2010) Steady open channel flows with curved streamlines: the Fawer approach revised. Environ Fluid Mech 10(3):297–310

50. Castro-Orgaz O, Chanson H (2011) Near-critical free surface flows: real fluid flow analysis. Environ Fluid Mech 11(5):499–516. https://doi.org/10.1007/s10652-010-9192-x
51. Viotti C, Carbone F, Dias F (2014) Conditions for extreme wave run-up on a vertical barrier by nonlinear dispersion. J Fluid Mech 748:768–788
52. Stoker JJ (1957) Water waves: the mathematical theories with applications. Wiley, New York
53. Friedrichs KO (1948) On the derivation of the shallow water theory. In: Stoker JJ (ed) The formation of breakers and bores, appendix. Communications on pure and applied mathematics, vol 1, pp 81–85
54. Montes JS (1986) A study of the undular jump profile. In: 9th Australasian fluid mech. conference Auckland, pp 148–151
55. Chanson H (2010) Undular tidal bores: basic theory and free-surface characteristics. J Hydraulic Eng 136(11):940–944
56. Leng X, Chanson H (2017) Upstream propagation of surges and bores: free-surface observations. Coastal Eng J 59(1):1750003. https://doi.org/10.1142/s0578563417500036
57. Koch C, Chanson H (2005) An experimental study of tidal bores and positive surges: Hydrodynamics and turbulence of the bore front, Department of civil engineering, The University of Queensland, Australia, Report CH56/05
58. Nikegbali P, Omidvar P (2018) Application of the SPH method to breaking and undular tidal bores on a movable bed. J Waterway Port Coastal Ocean Eng 144(2):04017040
59. Favre H (1935) Etude théorique et expérimentale des ondes de translation dans les canaux découverts. (Theoretical and experimental study of travelling surges in open channels). Dunod, Paris, France (in French)
60. Wang H, Chanson H (2015) Experimental study of turbulent fluctuations in hydraulic jumps. J Hydraulic Eng ASCE 141(7):04015010. https://doi.org/10.1061/(ASCE)HY.1943-7900.0001010)
61. Hoffman JD (2001) Numerical methods for engineers and scientists, 2nd edn. Marcel Dekker, New York
62. Ozmen-Cagatay H, Kocaman S (2010) Dam-break flows during initial stage using SWE and RANS approaches. J Hydraul Res 48(5):603–611
63. Castro-Orgaz O, Chanson H (2017) Ritter's dry-bed dam-break flows: positive and negative wave dynamics. Environ Fluid Mech 17(4):665–694
64. Kazolea M, Ricchiuto M (2018) On wave breaking for Boussinesq-type models. Ocean Model 123:16–39
65. Stansby PK, Chegini A, Barnes TCD (1998) The initial stages of dam-break flow. J Fluid Mech 374:407–424
66. Mohapatra PK, Eswaran V, Murthy Bhallamudi S (1999) Two-dimensional analysis of dam-break flow in a vertical plane. J Hydraulic Eng 125(2):183–192
67. Soares-Frazão S, Zech Y (2002) Undular bores and secondary waves: experiments and hybrid finite-volume modelling. J Hydraulic Res 40(1):33–43
68. Kiger KT, Duncan JH (2012) Air-entrainment mechanisms in plunging jets and breaking waves. Annu Rev Fluid Mech 44:563–596
69. Rao NSL, Kobus HE (1974) Characteristics of self-aerated free-surface flows. In: Water and waste water/current research and practice, vol 10. Eric Schmidt Verlag, Berlin
70. Chanson H (1997) Air bubble entrainment in free-surface turbulent shear flows. Academic Press, London
71. Ervine DA, Falvey HT (1987) Behaviour of turbulent water jets in the atmosphere and in plunge pools. In: Proceedings of the institution civil engineers, London, Part 2, vol 83, Mar 1987, pp 295–314
72. Chanson H, Leng X, Wang H (2019) Bubbles, transient turbulence and fish—challenging hydraulic structures of the 21st Century. In: Proceedings of 38th IAHR world congress, Panama City, 1–6 Sept, IAHR Publication, Lucas CALVO Ed., Plenary lecture
73. Barthelemy X, Banner ML, Peirson WL, Fedele F, Allis M, Dias F (2018) On a unified breaking onset threshold for gravity waves in deep and intermediate depth water. J Fluid Mech 841:463–488
74. Bacigaluppi P, Ricchiuto M, Bonneton P (2019) Implementation and evaluation of breaking detection criteria for a hybrid Boussinesq model. Water Waves. https://doi.org/10.1007/s42286-019-00023-8 (In print)
75. Benjamin TB, Lighthill MJ (1954) On cnoidal waves and bores. Proc Roy Soc Lond A 224:448–460